Article

Cancer Cell

The loss of RNA N^6-adenosine methyltransferase *Mettl14* in tumor-associated macrophages promotes $CD8^+$ T cell dysfunction and tumor growth

Graphical abstract

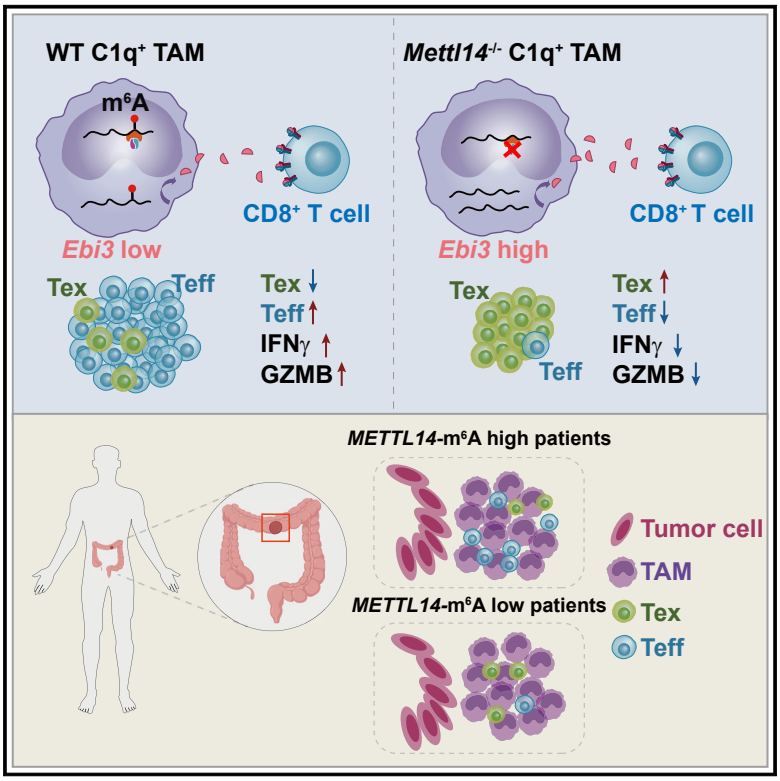

Highlights

- m^6A on mRNA directly controls the specification and function of the $C1q^+$ TAM
- *Mettl14* depletion in $C1q^+$ TAM promotes the growth of diverse solid tumors
- Macrophage-derived *Ebi3* transcript with decreased m^6A level drives T cell dysfunction
- *Mettl14* level in human tumor stroma is inversely correlated with T cell dysfunction

Authors

Lihui Dong, Chuanyuan Chen, Yawei Zhang, ..., Lin Shen, Meng Michelle Xu, Dali Han

Correspondence

michellexu@mail.tsinghua.edu.cn (M.M.X.), handl@big.ac.cn (D.H.)

In brief

Dong et al. discover an mRNA m^6A-mediated post-transcriptional regulatory mechanism in $C1q^+$ tumor-associated macrophages. The loss of *Mettl14* encoding an m^6A "writer" in these macrophages promotes the accumulation of *Ebi3* mRNA in an m^6A-dependent manner, thereby leading to $CD8^+$ T cell dysfunction and tumor growth.

Dong et al., 2021, Cancer Cell *39*, 1–13
July 12, 2021
https://doi.org/10.1016/j.ccell.2021.04.016

CellPress

Please cite this article in press as: Dong et al., The loss of RNA N^6-adenosine methyltransferase *Mettl14* in tumor-associated macrophages promotes $CD8^+$ T cell dysfunction and tumor growth, Cancer Cell (2021), https://doi.org/10.1016/j.ccell.2021.04.016

Cancer Cell

CellPress

Article

The loss of RNA N^6-adenosine methyltransferase *Mettl14* in tumor-associated macrophages promotes $CD8^+$ T cell dysfunction and tumor growth

Lihui Dong,[1,10] Chuanyuan Chen,[2,3,10] Yawei Zhang,[2,3,10] Peijin Guo,[1] Zhenghang Wang,[4] Jian Li,[4] Yi Liu,[1] Jun Liu,[5] Renbao Chang,[2,3] Yilin Li,[1] Guanghao Liang,[2,3] Weiyi Lai,[6] Mengxue Sun,[1] Urszula Dougherty,[7] Marc B. Bissonnette,[7] Hailin Wang,[6] Lin Shen,[4] Meng Michelle Xu,[1,*] and Dali Han[2,3,8,9,11,*]

[1]Department of Basic Medical Sciences, School of Medicine, Institute for Immunology, Beijing Key Lab for Immunological Research on Chronic Diseases, THU-PKU Center for Life Sciences, Tsinghua University, Beijing 100084, China

[2]Key Laboratory of Genomic and Precision Medicine, Beijing Institute of Genomics, and China National Center for Bioinformation, Chinese Academy of Sciences, Beijing 100101, China

[3]College of Future Technology, Sino-Danish College, University of Chinese Academy of Sciences, Beijing 100049, China

[4]Department of Gastrointestinal Oncology, Key Laboratory of Carcinogenesis and Translational Research (Ministry of Education), Peking University Cancer Hospital & Institute, Beijing 100142, China

[5]School of Life Sciences, Peking University, Beijing 100871, China

[6]State Key Laboratory of Environmental Chemistry and Ecotoxicology, Research Center for Eco-Environmental Sciences, Chinese Academy of Sciences, Beijing 100085, China

[7]Department of Medicine, The University of Chicago, Chicago, IL 60637, USA

[8]Institute for Stem Cell and Regeneration, Chinese Academy of Sciences, Beijing 100101, China

[9]China National Center for Bioinformation, Beijing, 100101, China

[10]These authors contributed equally

[11]Lead contact

*Correspondence: michellexu@mail.tsinghua.edu.cn (M.M.X.), handl@big.ac.cn (D.H.)

https://doi.org/10.1016/j.ccell.2021.04.016

SUMMARY

Tumor-associated macrophages (TAMs) can dampen the antitumor activity of T cells, yet the underlying mechanism remains incompletely understood. Here, we show that $C1q^+$ TAMs are regulated by an RNA N^6-methyladenosine (m^6A) program and modulate tumor-infiltrating $CD8^+$ T cells by expressing multiple immunomodulatory ligands. Macrophage-specific knockout of an m^6A methyltransferase *Mettl14* drives $CD8^+$ T cell differentiation along a dysfunctional trajectory, impairing $CD8^+$ T cells to eliminate tumors. *Mettl14*-deficient $C1q^+$ TAMs show a decreased m^6A abundance on and a higher level of transcripts of *Ebi3*, a cytokine subunit. In addition, neutralization of EBI3 leads to reinvigoration of dysfunctional $CD8^+$ T cells and overcomes immunosuppressive impact in mice. We show that the *METTL14*-m^6A levels are negatively correlated with dysfunctional T cell levels in patients with colorectal cancer, supporting the clinical relevance of this regulatory pathway. Thus, our study demonstrates how an m^6A methyltransferase in TAMs promotes $CD8^+$ T cell dysfunction and tumor progression.

INTRODUCTION

Recent advances in tumor immunotherapies aiming to reinvigorate tumor-infiltrating T cells have demonstrated clinical benefits in multiple types of cancer (Garon et al., 2015; Powles et al., 2014; Ribas and Wolchok, 2018; Wei et al., 2017). However, many patients do not respond to immunotherapies effectively due to the irreversibly dysfunctional state of T cells within the tumor microenvironment (TME) (Pauken et al., 2016; Philip et al., 2017; Sharma and Allison, 2015). The dysfunctional or exhausted state of tumor-infiltrating T cells is characterized by the lack of effector functions and the upregulation of inhibitory receptors, including programmed cell death-1 (PD-1), T cell immunoglobulin and mucin domain-3 protein (TIM-3), lymphocyte-activation gene 3 (LAG-3), T cell immunoglobulin and ITIM domain (TIGIT), and CD39, which are the hallmarks of exhaustion (McLane et al., 2019; Miller et al., 2019; Schietinger et al., 2016; Wherry et al., 2007). T cell dysfunction is induced by persistent antigen stimuli and influenced by T-cell-extrinsic factors within the TME, including the cytokines, chemokines, and metabolites derived from surrounding immunosuppressive populations (Schietinger et al., 2016; Thommen and Schumacher, 2018; Xia et al., 2019). However, some other factors, including cellular populations that drive and maintain the dysfunctional T cell, need to be further elucidated.

T cell function could be curtailed by myeloid cells within the TME. Myeloid cells, including macrophages and monocytes,

Please cite this article in press as: Dong et al., The loss of RNA N^6-adenosine methyltransferase *Mettl14* in tumor-associated macrophages promotes $CD8^+$ T cell dysfunction and tumor growth, Cancer Cell (2021), https://doi.org/10.1016/j.ccell.2021.04.016

are abundant in most types of tumors and are recognized as dominant populations in suppressing T cell function (Broz et al., 2014; DeNardo and Ruffell, 2019; Lavin et al., 2017). Macrophages and/or monocytes may overexpress programmed death-ligand 1 (PD-L1) and other ligands recognized by inhibitory receptors on T cells, thereby triggering T cell exhaustion (Cassetta et al., 2019; DeNardo and Ruffell, 2019; Tang et al., 2018). In addition, they may repress T cell function via secretion of regulatory cytokines such as interleukin-10 (IL-10) and transforming growth factor β (TGF-β) (DeNardo and Ruffell, 2019; Noy and Pollard, 2014; Ruffell et al., 2014; Speiser et al., 2016). It is demonstrated that tumor-associated macrophages (TAMs) are plastic and able to switch their function in response to environmental cues in the TME (Amit et al., 2016; Tzetzo and Abrams, 2021), resulting in functional heterogeneity with diverse phenotypes. Nevertheless, the functional phenotypes of macrophage subpopulations remain unclear and the underlying mechanism whereby macrophages govern T cell fate is not completely understood.

Transcriptional regulation coordinates with epi-transcriptional reprogramming, which ensures the specific patterns of gene expression and allows the phenotypic transition of TAMs (Locati et al., 2020). Emerging evidence reveals an additional layer of transcriptional control executed by RNA modification, particularly, N^6-methyladenosine (m^6A) methylation. As the most abundant modification in mRNA, m^6A is installed by the methyltransferase complex METTL3/METTL14/WTAP, and removed by the demethylases FTO and ALKBH5 (Jia et al., 2011; Liu et al., 2014; Nachtergaele and He, 2018; Ping et al., 2014; Zheng et al., 2013). When cells receive stimuli under different conditions, m^6A modifications can influence the half-life and translational efficacy of specific transcripts in a timely manner to effectively reprogram cellular phenotypes (Hsu et al., 2017; Liu et al., 2015; Shi et al., 2017; Wang et al., 2014, 2015). Growing evidence has demonstrated that the abundance of m^6A modification and the expression levels of m^6A modifiers are dysregulated in multiple types of cancers (Chang et al., 2020; Huang et al., 2020). Meanwhile, targeting of m^6A modifiers by small-molecule inhibitors exhibits a strong antitumor response and suppresses immune evasion by cancer cells (Huang et al., 2019; Su et al., 2020). These discoveries raise questions about whether RNA m^6A methylation in tumor-infiltrating immune cells directs a shift in their phenotypes and orchestrates an immunosuppressive TME to induce T cell dysfunction.

Here, we reveal that $C1q^+$ macrophages express a set of immunomodulatory ligands, and their function is regulated by the METTL14-YTHDF2 axis. *Mettl14* or *Ythdf2* deficiency in macrophages results in an impaired capacity to eliminate tumors by preventing cytotoxic T cell infiltration and promoting the accumulation of dysfunctional $CD8^+$ T cells. *Mettl14*-deficient macrophages exhibit a higher level of Epstein-Barr virus-induced protein 3 (*Ebi3*) transcripts that could promote dysfunctional T cell states. These results show that $C1q^+$ macrophages under the control of the METTL14-YTHDF2 axis maintain the equilibrium between cytotoxic and dysfunctional $CD8^+$ T cells, and unveil a potential therapeutic target to modulate the m^6A level in macrophages to rejuvenate T cell function.

RESULTS

Single-cell RNA sequencing reveals distinct phenotypes of tumor-associated macrophages and indicates macrophage-T cell cross talk

Tumor-infiltrating myeloid cells can fine-tune T cell function and limit the immunopathology of cytotoxic T cells to tissues, therefore providing an immune-privileged niche for tumor progression. Considering the phenotypic heterogeneity of myeloid cells, we performed single-cell RNA sequencing (scRNA-seq) to map myeloid subsets in the TME. Transcriptome profiling was performed on individual $CD45^+$ immune cells isolated from tumors of a Lewis lung carcinoma (LLC) mouse model (Figure S1A). We initially assessed the composition of tumor-infiltrating immune cells and identified distinct lineages on the basis of their signature genes, which included $CD4^+$ T cells, $CD8^+$ T cells, natural killer (NK) cells, dendritic cells (DCs), monocytes, and macrophages (Figures S1B and S1C). We then characterized gene signatures, and further stratified the monocytes and macrophages into three subsets (Figure 1A).

The first subset was identified as monocytes based on the high expression of *Ly6c2*, *Chil3*, and *Cybb* (Figures 1B, 1C, and S1D). Two remaining subsets were identified as macrophages, characterized by the abundant expression of *Cd9* and *Spp1* (Jaitin et al., 2019) and low expression of *Ly6c2* (Figures 1C and S1D): the Mac c1 subset expressed *Ptgs2*, *Ero1l*, and *Cxcl3*, resembling an angiogenic phenotype (Kale et al., 2014; Owen and Mohamadzadeh, 2013), and the Mac c2 subset expressed *C1qa*, *Cd81*, and *MHCII*, and this subset was previously demonstrated to be an immunomodulatory subset (Zhang et al., 2020) (Figures 1C and S1D). Functional enrichment analysis suggested that the Mac c1 subset (hereafter referred to $PTGS2^+$ macrophages) may function in angiogenesis and hypoxia. In contrast, the Mac c2 subset (hereafter referred to $C1q^+$ macrophages) was enriched for predicted functions in antigen presentation and had interferon γ (IFN-γ)-induced signatures, implying potential interplay between $C1q^+$ macrophages and surrounding IFN-γ-producing cells such as effector T cells (Figure 1D).

We then examined the potential cross talk between macrophage subsets and tumor-infiltrating $CD8^+$ T cells using the cell-cell communication analytical tools at CellPhoneDB (Efremova et al., 2020; Vento-Tormo et al., 2018). This indicated that interactions mediated through adhesion molecules were shared across the $PTGS2^+$ macrophage and $C1q^+$ macrophage subsets, reinforcing findings from prior reports about the adhesiveness of macrophages as a general mechanism affecting T cell retention within tissues (Egen et al., 2008; Peranzoni et al., 2018; Schlager et al., 2016) (Figure S1E). Analysis of specific ligand-receptor interactions revealed a unique pattern of interactions between $C1q^+$ macrophages and effector $CD8^+$ T cells ($CD8^+$ Teff) based on molecules associated with T cell recruitment and dysfunction (e.g., *Cxcl10*, *Nectin1*, and *Ebi3*) (Figure 1E).

Guided by these findings from single-cell analysis, we interrogated the potential significance of the $C1q^+$ macrophage subset in human cancer patients. Specifically, we examined the TCGA dataset for lung adenocarcinoma (LUAD) and used the signature mentioned above to infer the myeloid cell type abundance in the TME of individual patients. This revealed that tumors with more

Please cite this article in press as: Dong et al., The loss of RNA N^6-adenosine methyltransferase *Mettl14* in tumor-associated macrophages promotes $CD8^+$ T cell dysfunction and tumor growth, Cancer Cell (2021), https://doi.org/10.1016/j.ccell.2021.04.016

CellPress

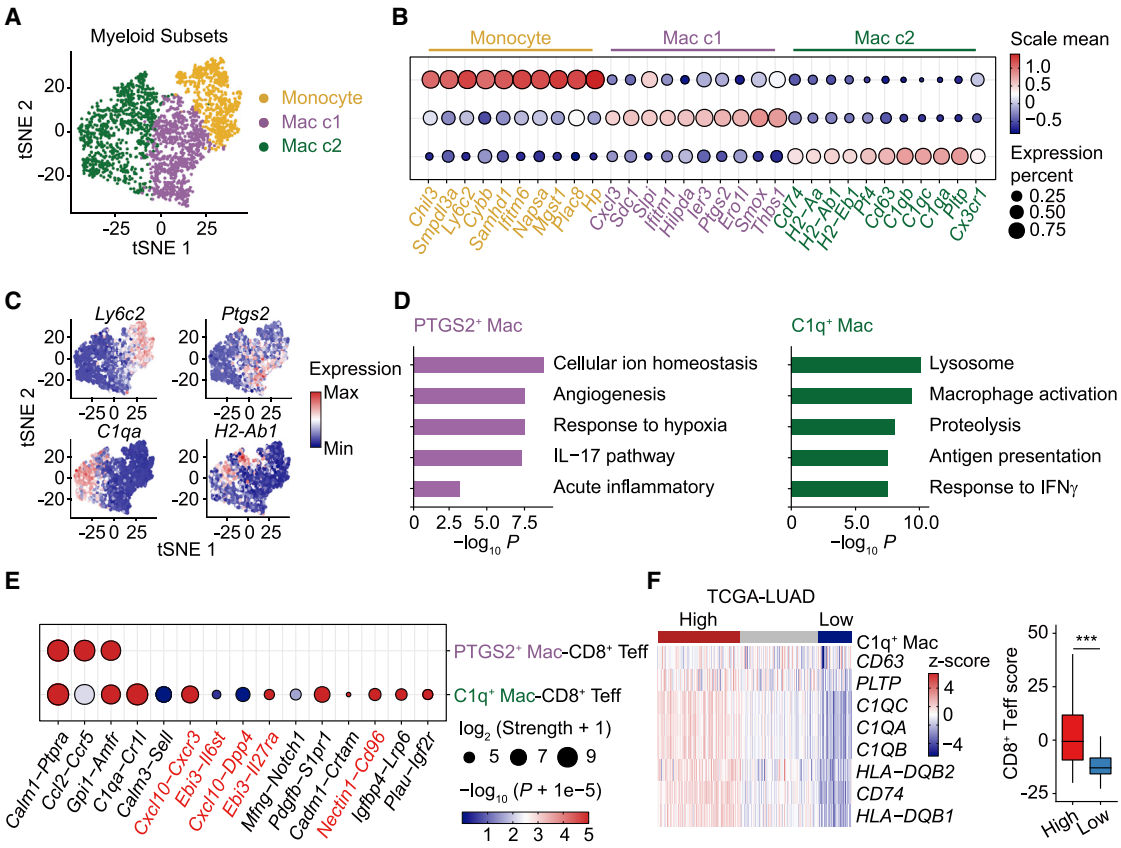

Figure 1. Characterization of tumor-associated macrophages by scRNA-seq

(A) A t-distributed stochastic neighbor embedding (t-SNE) plot displaying three clusters of myeloid cells from scRNA-seq, including the monocyte and two macrophage subsets (Mac c1 and Mac c2).

(B) Bubble heatmap showing the expression of representative genes for each subset shown in (A).

(C) Expression levels of selected genes in t-SNE space.

(D) Function enrichment analysis showing the functions of $PTGS2^+$ macrophage ($PTGS2^+$ Mac) and $C1q^+$ macrophage ($C1q^+$ Mac). Markers of $PTGS2^+$ Mac or $C1q^+$ Mac were used (cutoff: $\log_2$ [fold change] $\geq$0.25 and minimum detection rate $\geq$0.25).

(E) Bubble heatmap showing the mean attraction strength for selected ligand-receptor pairs between macrophages and effector $CD8^+$ T cells ($CD8^+$ Teff) from the scRNA-seq. Attraction strength was calculated by CellPhoneDB. Dot size indicates the attraction strength levels and colors show the p value calculated by permutation test.

(F) Patients from the TCGA-LUAD dataset were stratified by high and low expression of $C1q^+$ macrophages signatures. Color scale represents *Z*-score-normalized expression levels. Boxplot depicting the distributions of $CD8^+$ Teff infiltrating scores for patients in high and low groups (overall expression of *GZMA*, *GZMB*, *CD8A*, *CD8B*, and *PRF1*). Boxplot elements: center line, median; box limits, upper and lower quartiles; whiskers, 1%–99%. Statistical analysis was performed using the Wilcoxon rank-sum test. **p < 0.01.

See also Figure S1 and Table S1.

pronounced $C1q^+$ macrophage-like signatures often had strong $CD8^+$ Teff signatures, whereas there were no differences in $CD8^+$ Teff signatures in tumors carrying high and low $PTGS2^+$ macrophage-like signatures (Figures 1F and S1F). Our single-cell LLC data and TCGA analysis highlighted that $C1q^+$ macrophages express multiple immunomodulatory ligands and indicate that these ligands may functionally influence the recruitment of $CD8^+$ Teff.

$C1q^+$ macrophages are distinguished by a unique RNA m^6A methylation molecular phenotype

To understand whether the two observed macrophage subsets represent independent directions of differentiation in response to local stimuli, or perhaps rather different states along the same continuum of macrophage polarization or maturation, we next analyzed their differentiation trajectories. A URD analysis (Farrell et al., 2018) emphasized apparently strong directional flows for monocytes toward two differentiation trajectories (Figure 2A). Furthermore, analysis using a diffusion map algorithm (Coifman et al., 2005; Haghverdi et al., 2015) supported the idea that tumor-infiltrating monocytes may subsequently differentiate into $C1q^+$ or $PTGS2^+$ macrophages, apparently via distinct trajectories (Figures 2B and S2A).

We also focused on the trajectory-specific expression patterns of transcription factors and of known epigenetic regulators, seeking to identify regulatory molecules that may orchestrate the development of the two macrophage subsets. We noted that transcription factors driving "alternative activated" (M2) macrophage polarization (*Klf2* and *Klf4*) (Das et al., 2006; Liao et al., 2011) were elevated along the $C1q^+$ macrophage trajectory,

Please cite this article in press as: Dong et al., The loss of RNA N^6-adenosine methyltransferase *Mettl14* in tumor-associated macrophages promotes $CD8^+$ T cell dysfunction and tumor growth, Cancer Cell (2021), https://doi.org/10.1016/j.ccell.2021.04.016

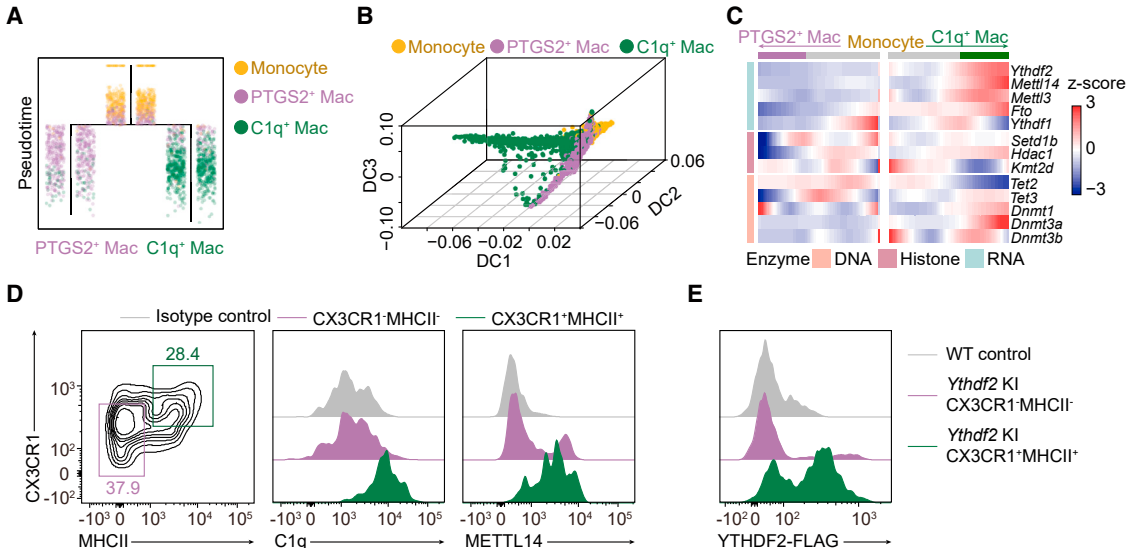

Figure 2. $C1q^+$ macrophage is distinguished by unique RNA m^6A methylation

(A and B) Inferred differentiation trajectory among three myeloid subsets from scRNA-seq by URD analysis (A) and diffusion map algorithm (B).

(C) Heatmap showing the transcriptional trends of epigenetic regulators along the diffusion components during the transition from monocyte to macrophage subsets. Color scale represents *Z*-score-normalized expression levels.

(D) Representative flow cytometry analysis of C1q and METTL14 expression in $CX3CR1^+MHCII^+$ and $CX3CR1^-MHCII^-$ TAMs from LLC-bearing wild-type mice.

(E) *Ythdf2*-KI and wild-type mice were subcutaneously injected with 5×10^5 LLC cells. Representative flow cytometry analysis of YTHDF2 expression in $CX3CR1^+MHCII^+$ and $CX3CR1^-MHCII^-$ TAMs. One of four representative experiments is shown (D and E).

See also Figure S2 and Table S2.

whereas $PTGS2^+$ macrophages expressed *Jun* and *Ets1* (Figure S2B). Notably, epigenetic regulators were preferentially expressed in $C1q^+$ macrophages (Figure 2C): the trajectory leading to $C1q^+$ macrophages included a gradual accumulation of two known writers of DNA methylation (*Dnmt1* and *Dnmt3a*) and downregulation of a DNA demethylase (*Tet2*) (Rodriguez-Ubreva et al., 2017; Wang et al., 2016). At the epi-transcriptomic regulatory level, we detected upregulation of RNA m^6A methylation-associated transcripts along the $C1q^+$ macrophage trajectory, including genes encoding methyltransferases (*Mettl3* and *Mettl14*), an m^6A reader protein (*Ythdf2*), and a demethylase (*Fto*) (Figure 2C).

To validate the expression of RNA m^6A methylation components in macrophages, we first sorted the two subsets based on their surface markers (CX3CR1 and MHCII) to discriminate $C1q^+$ macrophages ($CX3CR1^+MHCII^+$) and $PTGS2^+$ macrophages ($CX3CR1^-MHCII^-$). We performed bulk RNA-seq, excluding $Ly6C^{high}$ monocytes (Figure S2C), and found that the representative signature genes for the $C1q^+$ macrophages and $PTGS2^+$ macrophages from the scRNA-seq analysis were respectively recapitulated in the bulk-sorted $MHCII^+$ and $MHCII^-$ subsets (Figure S2D). Flow cytometry confirmed that $CX3CR1^{+-}$ $MHCII^+$ macrophages ($C1q^+$ macrophages) displayed much stronger C1q and METTL14 expression compared with $CX3CR1^-MHCII^-$ macrophages ($PTGS2^+$ macrophages) (Figure 2D). Indeed, $C1q^+$ TAMs had a significantly higher m^6A/A ratio compared with $PTGS2^+$ macrophages (Figure S2E). To further investigate YTHDF2 expression in macrophages, we constructed *Ythdf2*-3×FLAG-GGS-Avi-GGS knock-in (*Ythdf2* KI) mice, inserting a FLAG tag into the *Ythdf2* gene locus, to reflect YTHDF2 expression by detecting the expression level of FLAG (Figure S2F). Similar to C1q and METTL14, YTHDF2 is dominantly expressed in $CX3CR1^+MHCII^+$ macrophages (Figures 2E and S2G). Collectively, our predictive and confirmatory analyses of monocyte differentiation trajectories support the idea that the $C1q^+$ macrophage and $PTGS2^+$ macrophage subsets exhibit fundamentally distinct epigenetic regulatory impacts, and the $C1q^+$ subset's differentiation trajectory could be regulated by RNA m^6A methylation.

Mettl14 deficiency in macrophages promotes tumor growth and impedes $CD8^+$ T cell infiltration

To address the function of the METTL14-YTHDF2 regulatory axis in $C1q^+$ macrophages, we crossed $Mettl14^{flox/flox}$ mice with $LysM^{Cre}$ mice to delete *Mettl14* (hereafter $Mettl14^{flox/flox}$ denoted as wild type [WT] and $Mettl14^{flox/flox}LysM^{Cre}$ as *Mettl14* cKO). This deletion was more specific to macrophages, with minimal impacts on neutrophils or monocytes (Figure S3A), and the distribution of myeloid cells and lymphocytes was not affected in *Mettl14* cKO mice (Figures S3B–S3G). We found that B16-zsGreen-OTIp (B16-OZ) tumors grew significantly faster in *Mettl14* cKO mice than in WT mice (Figure 3A). In addition, B16F10 tumor cells with less overall immunogenicity also grew more aggressively in *Mettl14* cKO mice than in WT mice (Figure 3B). Similar results were also observed in experiments with mice bearing LLC and MC38 tumors (Figures 3C and 3D). Moreover, we observed a similar trend of accelerated tumor growth in *Mettl3* cKO mice ($Mettl3^{flox/flox}LysM^{Cre}$) (Figure S3H).

Considering the expression patterns of *Mettl14* and *Ythdf2*, specifically in $C1q^+$ macrophages, we reasoned that the downstream function of METTL14 might be mediated through the m^6A reader protein YTHDF2. Pursuing this, we compared the

Please cite this article in press as: Dong et al., The loss of RNA N^6-adenosine methyltransferase *Mettl14* in tumor-associated macrophages promotes $CD8^+$ T cell dysfunction and tumor growth, Cancer Cell (2021), https://doi.org/10.1016/j.ccell.2021.04.016

CellPress

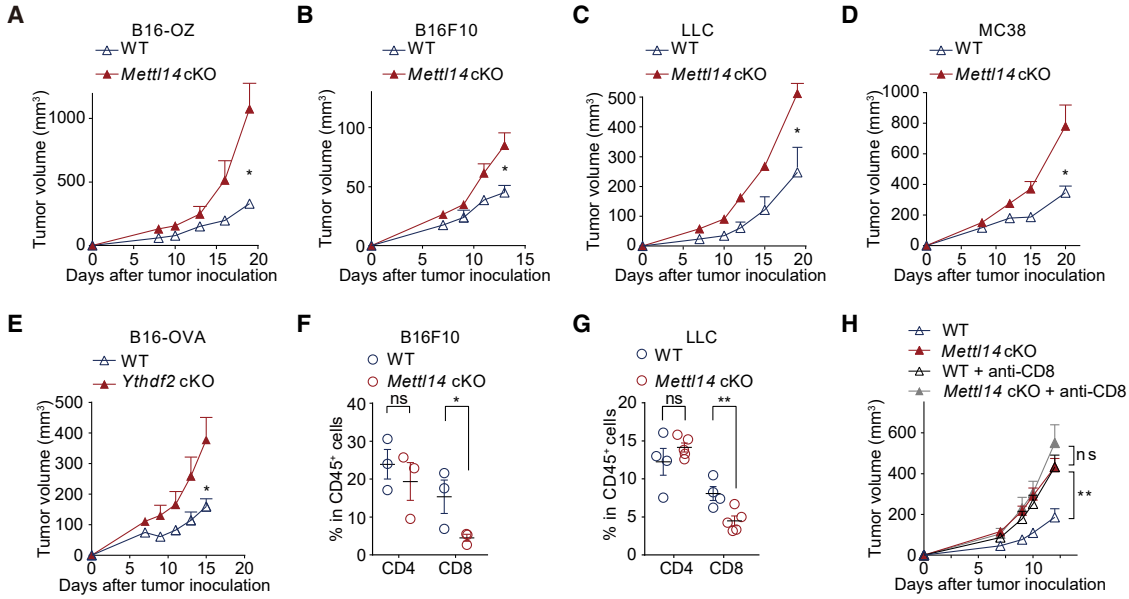

Figure 3. *Mettl14* deficiency in macrophage impairs the antitumor response and $CD8^+$ T cell infiltration

(A–D) WT (*Mettl14*$^{flox/flox}$, n = 4–6) and *Mettl14* cKO (*Mettl14*$^{flox/flox}$*LysM*^{Cre}, n = 4–6) mice were injected subcutaneously with 5 × 10^5 B16-zsGreen-OTIp (B16-OZ) (A), 10^5 B16F10 (B), 5 × 10^5 LLC (C), or 5 × 10^5 MC38 (D) cells.

(E) WT (*Ythdf2*$^{flox/flox}$, n = 5) and *Ythdf2* cKO (*Ythdf2*$^{flox/flox}$*LysM*^{Cre}, n = 5) mice were injected subcutaneously with 5 × 10^5 B16-OVA cells. All mice from two independent experiments were pooled together.

(F and G) Proportion of tumor-infiltrating $CD4^+$ and $CD8^+$ T cells among $CD45^+$ cells on day 12 post B16F10 tumor inoculation (F) and day 15 post LLC tumor inoculation (G) (B16F10, n = 3/group; LLC, n = 4–5/group).

(H) WT and *Mettl14* cKO mice were injected subcutaneously with 5 × 10^5 B16-OZ cells and administered intraperitoneally with 200 μg of CD8-depleting antibody on days −2 and 3 (n = 4–8/group). One of two representative experiments is shown (A–D and F–H).

n, number of mice; mean ± SEM; statistical analysis was performed using one-tailed (F and G) or two-tailed (A–E and H) unpaired *t* test. ns, non-significant, $p \geq 0.05$; *$p < 0.05$; **$p < 0.01$.

See also Figure S3 and Table S2.

tumor growth in *Ythdf2*$^{flox/flox}$ mice versus *Ythdf2* cKO mice (*Ythdf2*$^{flox/flox}$*LysM*^{Cre}). Consistent with our observation in *Mettl14* cKO mice, tumor growth was accelerated in *Ythdf2* cKO mice (Figures 3E and S3I). Thus, METTL14 and YTHDF2 may coordinately modulate TAM functions in a manner that affects tumor progression.

We next profiled the immune microenvironment of tumors from WT and *Mettl14* cKO mice. Experiments showed no apparent differences in the myeloid lineage compositions (including macrophage, DC, monocyte, and neutrophil) between WT and *Mettl14* cKO mice (Figure S3J), in agreement with previous observations (Lee et al., 2019). In addition, the proportion of $C1q^+$ TAMs and $PTGS2^+$ TAMs among $CD45^+$ cells did not differ between WT and *Mettl14* cKO mice (Figure S3K). Close examination of intratumoral DCs revealed that the distributions of both $CD103^+$ DCs and $CD11b^+$ DCs were similar in WT and *Mettl14* cKO mice, while DCs from WT and *Mettl14* cKO mice expressed comparable levels of MHCI, MHCII, CD86, and PD-L1 (Figures S3L and S3M). However, the proportion of $CD8^+$ T cells was significantly decreased in the *Mettl14* cKO mice (Figures 3F, 3G, S3N, and S3O). A similar decrease of tumor-infiltrating $CD8^+$ T cells was detected in the *Ythdf2* cKO mice (Figure S3P). We thus depleted $CD8^+$ T cells and evaluated whether the difference in tumor growth between WT and *Mettl14* cKO mice can be attributed to $CD8^+$ T-cell-mediated antitumor immunity. The tumor growth kinetics were comparable between WT and *Mettl14* cKO mice in the absence of $CD8^+$ T cells (Figure 3H). These findings suggest that loss of *Mettl14* in macrophages accelerates tumor progression by restricting $CD8^+$ T cells within the TME.

Loss of METTL14 in macrophages triggers a shift of intratumoral $CD8^+$ T cells toward a dysfunctional state

We next performed scRNA-seq on immune cells isolated from B16-OVA tumors established in WT and *Mettl14* cKO mice to monitor how macrophage-specific *Mettl14* knockout altered the intratumoral $CD8^+$ T cell population. We initially identified eight immune cell populations on the basis of their signature genes, which included macrophages, monocytes, NK cells, $CD4^+$ T cells, $CD8^+$ T cells, B cells, DCs, and other cells (Figures S4A and S4B). Transcriptional profiles of $CD8^+$ T cells revealed five discrete subpopulations (Figure 4A). An effector-like $CD8^+$ T cell subpopulation was marked by transcripts including *Ifng* and *Klrd1* ($CD8^+$ Teff), whereas a progenitor-like $CD8^+$ T cell subpopulation expressed genes including *Tcf7* and *Bcl2* ($CD8^+$ progenitor; Figures 4A and S4C). There was also a Tox^+ subpopulation ($CD8^+$ Tex) characterized by expression of transcription factors known to function in exhausted T cells (e.g., *Tox* and *Nfatc1*; Figures 4A and S4C), and a cycling subpopulation ($CD8^+$ Tex cycling) marked by high expression of both exhaustion-associated markers and classic markers for S phase (*E2f8* and *Cdc45*) and G2/M phase (*Cks2* and *Ccnb2*; Figures S4C

Please cite this article in press as: Dong et al., The loss of RNA N^6-adenosine methyltransferase *Mettl14* in tumor-associated macrophages promotes CD8$^+$ T cell dysfunction and tumor growth, Cancer Cell (2021), https://doi.org/10.1016/j.ccell.2021.04.016

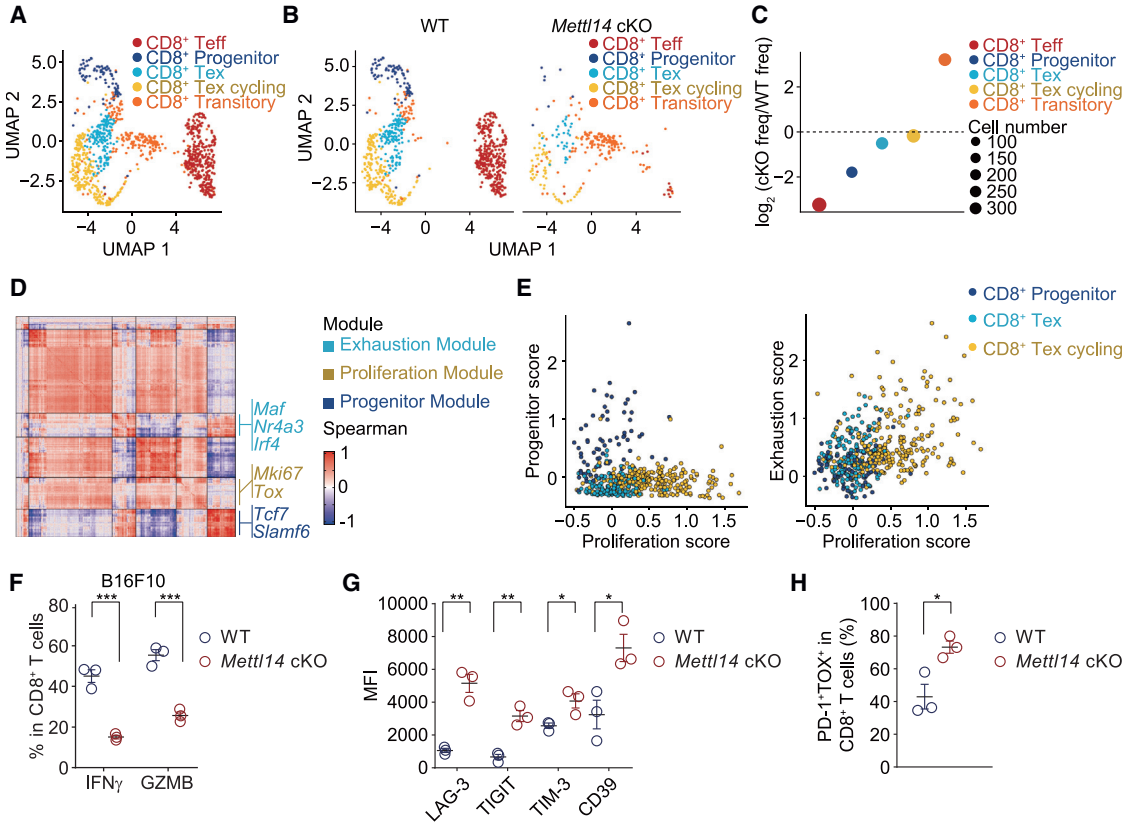

Figure 4. Divergent CD8$^+$ T cell differentiation is controlled by METTL14-dominated macrophage

(A) CD45$^+$ immune cells were sorted on day 9 post B16-OVA inoculation followed by scRNA-seq. Uniform manifold approximation and projection (UMAP) plot showing five subpopulations of tumor-infiltrating CD8$^+$ T cells in WT and *Mettl14* cKO mice.

(B) Distribution of CD8$^+$ T cell subpopulations across WT and *Mettl14* cKO mice.

(C) Dot plot depicting the relative frequency of each CD8$^+$ T cell subpopulation between WT and *Mettl14* cKO mice.

(D) Heatmap of gene co-expression modules for top variable genes within CD8$^+$ T cells. Colors represented the Spearman correlation coefficient.

(E) Scatterplots depicting the proliferation score (top 20 genes most correlated with *Tox*) versus the scores of exhaustion (top 20 genes most correlated with *Nr4a3*) and progenitor (top 20 genes most correlated with *Tcf7*) per cell.

(F–H) WT (n = 3) and *Mettl14* cKO (n = 3) mice were injected subcutaneously with 10^5 B16F10 cells. Flow cytometry analysis of IFN-γ and GZMB production in tumor-infiltrating CD8$^+$ T cells 12 days after tumor inoculation (F). The mean fluorescence intensity (MFI) of co-inhibitory receptors on tumor-infiltrating CD8$^+$ T cells (G). The frequency of PD-1$^+$TOX$^+$ CD8$^+$ T cells is shown (H). One of two representative experiments is shown (F–H).

n, number of mice; mean ± SEM; statistical analysis was performed using two-tailed unpaired *t* test. *p < 0.05; **p < 0.01; ***p < 0.001.

See also Figure S4, Tables S1 and S2.

and S4D). The final subpopulation featured enriched expression of *Btg2* and *Junb*, and the absence of the activation marker *Cd69*, features collectively resembling a transitory state with insufficient activation (CD8$^+$ transitory; Figures 4A and S4C).

We next compared the abundance of each subpopulation in WT and *Mettl14* cKO mice. We noticed that CD8$^+$ progenitor and CD8$^+$ Teff diminished in *Mettl14* cKO mice, whereas the CD8$^+$ transitory subpopulation was predominant in *Mettl14* cKO mice (Figures 4B and 4C). To infer the relationship between CD8$^+$ Teff and CD8$^+$ transitory subpopulations, we used the diffusion map to model CD8$^+$ T cell fate commitment (Figure S4E). Although CD8$^+$ transitory and CD8$^+$ Teff subpopulations showed close relatedness with DC1 and DC2 (diffusion components 1 and 2), these two subpopulations could be distinguished by DC3 (diffusion component 3) (Figure S4E). Specifically, the CD8$^+$ transitory subpopulation showed higher expression of glycolysis-associated genes and lower expression of activation genes than the CD8$^+$ Teff subpopulation (Figure S4F), reflecting an aberrant activation of the transitory subpopulation enriched in the *Mettl14* cKO condition.

To further delineate the transcriptional divergence of three continuous CD8$^+$ T cell populations (CD8$^+$ progenitor, CD8$^+$ Tex, and CD8$^+$ Tex cycling) on the diffusion map in WT and *Mettl14* cKO mice, we performed gene co-expression analysis across CD8$^+$ T cells. We identified several co-regulated gene modules (Figure 4D), which revealed apparent programs related to proliferation (*Mki67* and *Tox*, proliferation module), transcriptional factors linked to exhaustion (*Maf*, *Nr4a3*, and *Irf4*, exhaustion module), and progenitor T cell markers (*Tcf7* and *Slamf6*, progenitor module; Figure 4D). We next compared the distribution of T cell subpopulations by computing three transcriptional scores to quantify: (1) the progenitor state, (2) the proliferation state, and (3) the exhaustion state. We noticed that the CD8$^+$ progenitor subpopulation displayed higher progenitor scores

Please cite this article in press as: Dong et al., The loss of RNA N^6-adenosine methyltransferase *Mettl14* in tumor-associated macrophages promotes $CD8^+$ T cell dysfunction and tumor growth, Cancer Cell (2021), https://doi.org/10.1016/j.ccell.2021.04.016

than $CD8^+$ Tex and comparable exhaustion scores to $CD8^+$ Tex, reinforcing $CD8^+$ progenitors as the progenitor-exhausted $CD8^+$ T cells (Figures 4E and S4G). Indeed, visualization of the exhaustion and proliferation scores revealed a continuum of differentiation/exhaustion from $CD8^+$ progenitor to $CD8^+$ Tex cycling (Figure 4E). Together, these results suggest that *Mettl14* deficiency in macrophages abolishes the maintenance of progenitor-exhausted $CD8^+$ T cells and directs T cell differentiation toward a dysfunctional trajectory.

We next validated functional phenotypes of tumor-infiltrating $CD8^+$ T cells by assessing their capacity to produce IFN-γ and GZMB. Flow cytometry analysis showed that cytokine production of $CD8^+$ T cells from B16F10 and/or B16-OZ tumors was impaired in *Mettl14* cKO mice (Figures 4F and S4H). However, the cytokine-producing capacity of $CD4^+$ T cells did not differ between WT and *Mettl14* cKO mice (Figure S4I). In addition, the expression of co-inhibitory receptors known as hallmarks of an exhausted T phenotype, such as LAG-3, TIGIT, TIM-3, and CD39 (Blackburn et al., 2009; Kuchroo et al., 2014; Wherry et al., 2007), was substantially increased in *Mettl14* cKO mice (Figure 4G). We further confirmed these findings in LLC and MC38 tumor models (Figures S4J–S4M). Meanwhile, the proportion of Ki-67^+ $CD8^+$ T cells and the expression of the antiapoptotic molecule BCL-2 was significantly reduced in $CD8^+$ T cells from *Mettl14* cKO mice compared with WT mice, supporting the idea that the observed reduction in $CD8^+$ T cells within the tumor of *Mettl14* cKO mice can be attributed to a combination of reduced expansion and elevated vulnerability to apoptosis (Figures S4N and S4O).

We also noted that expression of the transcription factor *Tox* (Khan et al., 2019), the center regulator of T cell exhaustion, was consistently elevated in tumor-infiltrating $CD8^+$ T cells from *Mettl14* cKO mice, implicating transcriptional control of exhausted T cell commitment in the *Mettl14* cKO condition (Figures 4H and S4P). We then confirmed these findings in an orthotopic lung cancer model by injecting LLC tumor cells intravenously into WT and *Mettl14* cKO mice (Figures S4Q–S4T). To test whether *Mettl14* deficiency in macrophages leads to $CD8^+$ T cell dysfunction, we isolated tumor-associated $C1q^+$ and $PTGS2^+$ macrophages and co-cultured them with OT-I T cells. Decreased IFN-γ production was observed for the $CD8^+$ T cells co-cultured with *Mettl14*-deficient $C1q^+$ TAMs compared with the $CD8^+$ T cells co-cultured with WT $C1q^+$ TAMs. However, no similar trends were observed upon co-culturing with $PTGS2^+$ TAMs (Figure S4U). Together, these data suggest that loss of *Mettl14* in macrophages controls the bifurcation between divergent $CD8^+$ T cell fates, driving $CD8^+$ T cell dysfunction and repressing $CD8^+$ Teff activation.

Macrophage-derived *Ebi3* mRNA transcripts with altered m^6A methylation drive impaired antitumor T cell responses

Our findings support the hypothesis that a macrophage-specific, m^6A-mediated process may orchestrate the dysfunction of intratumoral $CD8^+$ T cells. We initially confirmed that *Mettl14*-deficient bone marrow-derived macrophages (BMDMs) had a significantly decreased m^6A/A ratio compared with WT BMDMs (Figure S5A). We next examined the *in vivo* context by sorting TAMs from WT and *Mettl14* cKO mice and performing m^6A sequencing. Macrophages from *Mettl14* cKO mice exhibited an apparent decrease in m^6A methylation compared with macrophages from WT mice (Figures 5A, 5B, and S5B). Recalling that the METTL14-YTHDF2 regulatory axis destabilizes m^6A-marked transcripts (Wang et al., 2014), we compared the abundance of m^6A-marked mRNAs following *Mettl14* depletion with non-m^6A-marked mRNAs. Our comparison of TAMs isolated from both LLC and B16-OVA tumors revealed a significant increase in m^6A-marked mRNAs following the knockout of *Mettl14*, as reflected by a right shift in the cumulative fraction of these transcripts compared with non-m^6A-marked mRNAs (Figures 5C and S5C).

We next interrogated which genes under the control of m^6A methylation in $C1q^+$ macrophages led to the dysfunctional phenotype of $CD8^+$ T cells. Since genes in response to IFN-γ and antigen presentation pathways were highly expressed in $C1q^+$ TAMs and might be involved in regulating $CD8^+$ T cell response (Jerby-Arnon et al., 2018), we initially compared the expression levels of genes from these two pathways in WT and *Mettl14* cKO TAMs isolated from both LLC and B16-OVA tumor models. There was no significant difference in transcriptional and protein levels of IFN-γ-stimulating genes, antigen-presentation genes, or MHC-related genes detected between WT and *Mettl14* cKO (Figures S5D–S5F). Given the critical roles of immunoregulatory ligands in determining T cell function, we reexamined the aforementioned ligands that are involved in macrophage-T cell cross talk and expressed specifically by $C1q^+$ macrophages (Figure 1E). We found that several m^6A-marked immunoregulatory ligands showed elevated expression based on the ranking fold change of mRNA abundance in *Mettl14* cKO TAMs (Figures 5D and S5G). Most obviously, we found that *Ebi3*, a subunit of both of the heterodimeric cytokines IL-27 and IL-35, which were demonstrated to induce T cell exhaustion (Sawant et al., 2019; Turnis et al., 2016; Vignali and Kuchroo, 2012), was strongly upregulated in *Mettl14* cKO macrophages in both LLC and B16-OVA tumors (Figures 5D and S5G). We also observed that the m^6A abundance of *Ebi3* was remarkably decreased in *Mettl14* cKO macrophages ($p = 3.8 \times 10^{-3}$, likelihood ratio test) (Figures 5D, S5G, and S5H), clearly suggesting that *Mettl14* in macrophages controls *Ebi3* in an m^6A-dependent manner. We next examined *Ebi3* mRNA and protein levels in macrophages and observed significant accumulation of EBI3 in the $C1q^+$ macrophage in tumors of *Mettl14* cKO mice (Figures 5E and S5I). Consistently, the EBI3 protein level was elevated in *Ythdf2*-deficient macrophages compared with WT macrophages (Figure S5J).

To evaluate the impact of EBI3 on tumor growth, we treated tumor-bearing mice with an anti-EBI3 neutralizing antibody. As expected, the tumors of *Mettl14* cKO mice grew rapidly. However, the amounts of tumor growth were similar between WT and *Mettl14* cKO mice given this EBI3-neutralizing antibody (Figure 5F). We also depleted $CD8^+$ T cells and observed that the EBI3 neutralization-induced reduction in tumor growth was entirely abrogated in the absence of $CD8^+$ T cells, indicating that $CD8^+$ T cells are essential for the improved antitumor response following EBI3 blockade (Figure 5F). Indeed, neutralization of EBI3 markedly rescued the impaired IFN-γ

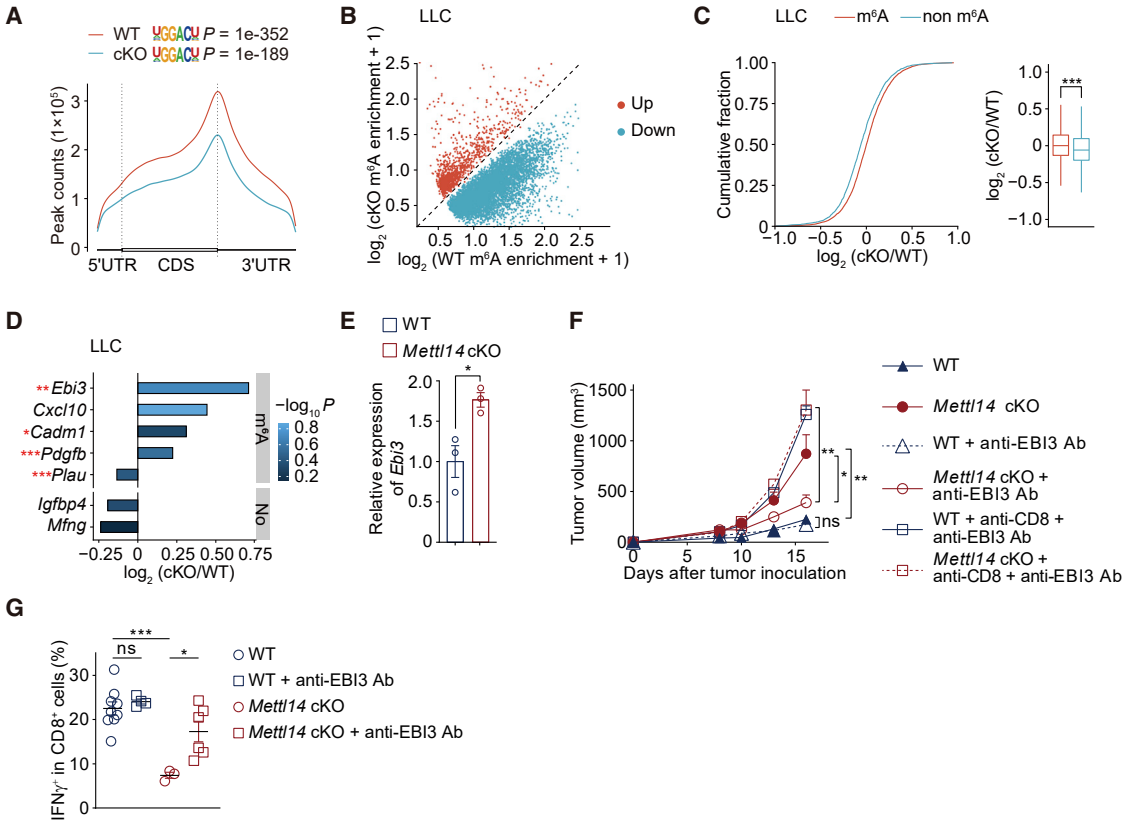

Figure 5. Epi-transcriptome analysis identified *Ebi3* as an m^6A-modified differentially expressed gene in *Mettl14* cKO macrophages

(A) Metagene distribution of the m^6A peaks of TAMs along the whole transcriptome. TAMs were isolated from WT (n = 3) and *Mettl14* cKO (n = 2) mice on day 16 post LLC inoculation. The enriched consensus motifs were detected within m^6A peaks. Statistical analyses were performed using one-tailed binomial test.

(B) Scatterplot showing the m^6A enrichment in identified m^6A peaks of TAMs. Peaks with significantly increased and decreased m^6A enrichment are highlighted in red and blue, respectively.

(C) Cumulative distribution and boxplot (right) representing the expression changes in transcripts with or without m^6A peaks between WT (n = 4) and *Mettl14* cKO (n = 2) TAMs isolated from LLC-bearing mice. Boxplot elements: center line, median; box limits, upper and lower quartiles; whiskers, 1%–99%. Statistical analysis was performed using two-tailed Kolmogorov-Smirnov test.

(D) Bar plot representing the differential expression of ligands involved in macrophage-T cell cross talk and expressed explicitly by $C1q^+$ macrophages, in WT (n = 4) and *Mettl14* cKO (n = 2) TAMs. The p values for difference in gene expression were calculated by Wald test. Asterisks represent genes that contain m^6A peaks with significant changes.

(E) $CX3CR1^+MHCII^+$ TAMs from LLC-bearing WT and *Mettl14* cKO mice were sorted on day 14. The mRNA level of *Ebi3* (relative to *Actb*) was evaluated using real-time qPCR.

(F) WT and *Mettl14* cKO mice were injected subcutaneously with 5×10^5 B16-OZ cells. Tumor-bearing mice were intratumorally injected with anti-EBI3 neutralizing antibody (4 μg) on days 8 and 10. Two hundred micrograms of CD8-depleting antibody was injected intraperitoneally on days 8 and 10 (n = 4–6/group).

(G) Flow cytometry analysis of IFN-γ production in tumor-infiltrating $CD8^+$ T cells isolated from WT (n = 9), *Mettl14* cKO (n = 3), WT + anti-EBI3 Ab (n = 4), and *Mettl14* cKO + anti-EBI3 Ab mice (n = 6) 16 days post B16-OZ inoculation. One of two representative experiments is shown (E–G).

n, number of mice; mean ± SEM; two-tailed unpaired *t* test. ns, non-significant, $p \geq 0.05$; *$p < 0.05$; **$p < 0.01$; ***$p < 0.001$.

See also Figure S5, Tables S2, S3, and S4.

production in $CD8^+$ T cells from *Mettl14* cKO mice (Figure 5G). To help functionally link EBI3 to $CD8^+$ T cell dysfunction, we activated naive OT-I T cells in the presence or absence of IL-35. T cells receiving IL-35 treatment showed less IFN-γ production compared with T cells without treatment (Figure S5K). Therefore, these findings support the idea that METTL14-mediated m^6A methylation on *Ebi3* within $C1q^+$ macrophages serves as a switch shifting the TME toward an immunosuppressive phenotype. Blocking EBI3's negative regulation of T cell function overcomes the immunosuppressive impact of *Mettl14* loss in TAMs.

Reduced METTL14 expression and m^6A level in tumor stromal cells is associated with decreased T cell infiltration in colon cancer patients

To determine whether these insights about METTL14 regulation can translate to human patients' tumor samples, we examined the protein level of METTL14 through immunohistochemical staining of tumor tissues from colon cancer patients. We found that approximately 60% of $METLL14^+$ cells in the surrounding tumor stroma were stained positively for macrophage marker CD68, and METTL14 was localized in the nucleus of $CD68^+$ macrophages (Figures 6A and S6A). Further, the mRNA level of

Please cite this article in press as: Dong et al., The loss of RNA N^6-adenosine methyltransferase *Mettl14* in tumor-associated macrophages promotes $CD8^+$ T cell dysfunction and tumor growth, Cancer Cell (2021), https://doi.org/10.1016/j.ccell.2021.04.016

METTL14 and the overall m^6A level were strongly correlated (Figure 6B). Notably, the overall m^6A level was significantly decreased in tumor stromal cells compared with stromal cells of matched samples from healthy controls (Figure 6C). Also, the overall m^6A level in tumor stromal cells was positively correlated with the *CD8A* transcript level, implying that an increase in m^6A was somehow functionally related to the degree of $CD8^+$ T cell infiltration within the TME (Figure 6D). Bulk RNA-seq further validated that patients with lower m^6A levels showed lower effector T cell signatures ($CD8^+$ Teff) and higher exhausted T cell signatures ($CD8^+$ Tex; Figure 6E). To gain more insight into the spatial distribution of macrophages and T cells, we conducted multi-color immunohistochemistry (IHC) and observed that $EBI3^+$ macrophages were close to $CD8^+$ T cells in the colon cancer patient, implying a potential interplay between macrophages and surrounding $CD8^+$ T cells in the TME (Figures 6F and S6B).

To extend the above findings to melanoma and non-small cell lung cancer cases, we analyzed public scRNA-seq datasets (Kim et al., 2020; Sade-Feldman et al., 2018) and confirmed that the expression levels of *METTL14* and *YTHDF2* did gradually increase along the $C1q^+$ Mac trajectory (Figures S6C, S6D, S6H, and S6I). In addition, we noted directly opposing expression trends for *METTL14* and *EBI3* throughout the middle and later phases of the $C1q^+$ Mac trajectory (Figures S6D and S6I). The *EBI3* expression level in macrophages was positively correlated with the proportion of exhausted $CD8^+$ T cells (Figures S6E–S6G). In line with our results from multiple mouse models, these data from clinical tumor samples further support that loss of m^6A in tumor stromal cells is mediated by downregulation of *METTL14* expression, and this m^6A reduction may restrict antitumor T cell response in the TME.

DISCUSSION

An immunosuppressive TME both prevents T cell cytotoxicity and promotes T cell dysfunction, resulting in compromised antitumor responses and tumor escape from immune surveillance. Macrophages are dominant mediators that drive immunosuppression, doing so via direct and indirect mechanisms. However, it is not clear which macrophage subpopulation(s) interacts with T cells within tumors, so it has been difficult to functionally dissect the interplay between macrophages and T cells in the TME. Here, we reveal that (1) $C1q^+$ TAMs specifically express ligands that cross talk with intratumoral T cells; (2) METTL14 and YTHDF2 are specifically enriched in $C1q^+$ TAMs, which in turn maintain the equilibrium of cytotoxic $CD8^+$ T cells and dysfunctional $CD8^+$ T cells; (3) the accumulation of dysfunctional $CD8^+$ T cells results from m^6A-dependent increased EBI3 expression in intratumoral macrophages from *Mettl14*-deficient mice; and (4) the m^6A level in the TME of human patients showed a positive correlation with the level of $CD8^+$ T cell infiltration and the effector functions of $CD8^+$ T cells.

Considering the significant functional impacts of macrophages on T cell function and antitumor immunity, extensive research has attempted to identify molecular regulators that could repolarize macrophages from a suppressive into a stimulatory element. Traditionally, the focus has been on effects of genetic variation, for example, the finding that IRF8 expression in TAMs drives T cell exhaustion phenotypes through their antigen-presenting function (Nixon et al., 2020). More recently, the epigenetic regulation processes orchestrating macrophage flexibility have become a research hotspot. A study showed that an HDAC inhibitor induced the recruitment and differentiation of highly phagocytic and stimulatory macrophages within tumors and showed inhibition of breast tumors and metastases (Guerriero et al., 2017). We speculated the epi-transcriptional regulation functions as an additional mechanistic layer directing the immunosuppressive capacity of macrophages. The mRNA m^6A mediators METTL14 and YTHDF2 within TAMs alter the abundance of a set of m^6A-regulated proteins such as EBI3 that determine T cell phenotypes in tumors in response to environmental cues provided by surrounding T cells.

Thus, understanding the METTL14-YTHDF2-driven epi-transcriptomic regulation within the TME suggests paths for the development of potential immunotherapies targeting macrophages. Moreover, blocking the downstream mediators, such as EBI3, to restrict T cell dysfunction and maximize responsiveness to immune checkpoint blockade should be considered in the future.

STAR★METHODS

Detailed methods are provided in the online version of this paper and include the following:

- KEY RESOURCES TABLE
- RESOURCE AVAILABILITY
  - Lead contact
  - Materials availability
  - Data and code availability
- EXPERIMENTAL MODEL AND SUBJECT DETAILS
  - Mice
  - Cell line
  - *Ythdf2*-3×Flag-GGS-Avi-GGS knock-in mouse lineage establishment
  - Human specimens
- METHOD DETAILS
  - Mouse genotyping
  - Tumor growth and treatment
  - Flow cytometry and cell sorting
  - Cytokine detection of tumor-infiltrating T cells
  - Co-culture assay for macrophages and T cells
  - *In vitro* T cells and macrophages treatment
  - Measurement of IFNγ-secreting $CD8^+$ T cells by ELISPOT assay
  - Orthotopic lung tumor model induction and tissue processing
  - Bone marrow-derived macrophage induction
  - DNA/RNA extraction and qPCR analysis for gene expression
  - UHPLC-MRM-MS/MS analysis of mononucleotides for m^6A level quantification
  - Immunohistochemistry of human biopsies
  - Multi-color IHC
  - RNA-seq and m^6A-seq
  - Single-cell RNA-seq
  - Single-cell RNA-seq analysis

Please cite this article in press as: Dong et al., The loss of RNA N^6-adenosine methyltransferase *Mettl14* in tumor-associated macrophages promotes $CD8^+$ T cell dysfunction and tumor growth, Cancer Cell (2021), https://doi.org/10.1016/j.ccell.2021.04.016

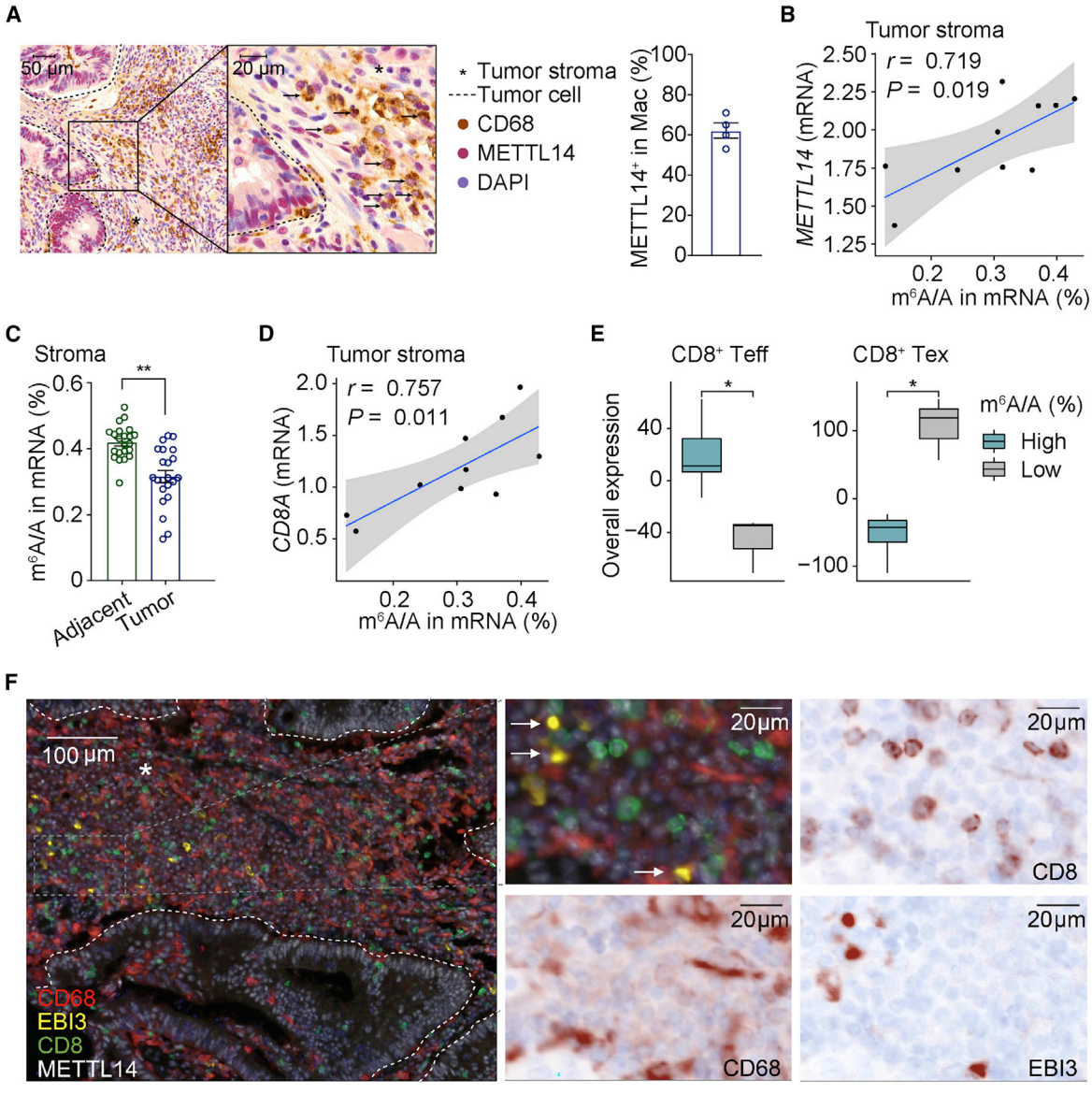

Figure 6. Reduced METTL14 expression and m^6A level in tumor stromal cells are associated with decreased T cell infiltration in colon cancer patients

(A) Tissue sections from patients with colon cancer were immunohistochemically stained for macrophage marker CD68 (brown) and METTL14 (red). The arrows indicate the CD68 and METTL14 double-positive cells. The dashed line shows the edge of the tumor. Asterisks mark the stroma. Scale bars, 50 or 20 μm. Right: bar plot showing the proportion of $METTL14^+$ macrophages in total macrophages.

(B) Pearson's correlation between *METTL14* transcripts (log-transformation) and m^6A level in tumor stromal cells is shown (n = 10). The shaded area represents the 95% confidence interval.

(C) Quantification of the m^6A level in mRNAs isolated from adjacent stromal and tumor stromal cells (n = 22). The p value was calculated by two-tailed paired *t* test.

(D) Pearson's correlation between *CD8A* transcripts (log-transformation) and m^6A level in tumor stroma is shown (n = 10). The shaded area represents the 95% confidence interval.

(E) Boxplots depicting the overall expression of $CD8^+$ Teff and $CD8^+$ Tex signatures for patients in high (blue) and low (gray) m^6A groups (n = 10; the cutoff of low m^6A was m^6A/A (%) < 0.3). The expression of $CD8^+$ Teff and $CD8^+$ Tex signatures (from B16-OVA scRNA-seq data) was quantified by RNA-seq. Boxplot elements: center line, median; box limits, upper and lower quartiles; whiskers, 1%–99%. Statistical analysis was performed using the Wilcoxon rank-sum test.

(F) Representative example of colorectal cancer stained by multi-color IHC. The staining images indicate EBI3 (yellow), METTL14 (white), CD68 (red), CD8 (green), and DAPI (blue). The arrows indicate the CD68 and EBI3 double-positive cells within the tumor stroma. The dashed line shows the edge of the tumor. The asterisk marks the stroma. Scale bars, 100 or 20 μm.

n, number of patients; mean ± SEM; *r* represents the Pearson's correlation coefficient; *p < 0.05; **p < 0.01.

See also Figure S6 and Table S5.

- Ligand and receptor interaction analysis
- Trajectory interference
- Gene co-expression module analysis
- Bulk RNA-seq analysis
- m^6A-seq analysis
- TCGA expression data analysis
- Public single cell data analysis

- QUANTIFICATION AND STATISTICAL ANALYSIS

SUPPLEMENTAL INFORMATION

Supplemental information can be found online at https://doi.org/10.1016/j.ccell.2021.04.016.

ACKNOWLEDGMENTS

This work was funded by the National Key R&D Program of China (2018YFA0109700 to D.H.), Strategic Priority Research Program (XDA16010115 to D.H.), National Science Fund for Excellent Young Scholars (81922054 to M.M.X. and 31922017 to D.H.), Beijing Natural Science Foundation (Z200023 to M.M.X. and Z190016 to D.H.), the Key Research Program of Frontier Sciences, Chinese Academy of Sciences (ZDBS-LY-SM013 to D.H.), and CAS Hundred Talent Program (to D.H.).

AUTHOR CONTRIBUTIONS

D.H. and M.M.X. conceived the project. L.D. and J.G. performed most of the experiments under the supervision of M.M.X. C.C. and Y.Z. performed most of the bioinformatics analysis under the supervision of D.H. Z.W., J. Liu, J. Li, U.D., M.B.B., and L.S. provided human specimens. Y.L. performed IHC staining. Y.-L.L., R.C., and M.S. helped to perform animal experiments. C.C. and G.L. performed m^6A-sequencing data analysis. W.L. and H.W. performed UHPLC-MRM-MS/MS analysis. D.H. and M.M.X. designed the study. D.H., M.M.X., L.D., C.C., and Y.Z. wrote the manuscript with input from all authors.

DECLARATION OF INTERESTS

The authors declare no competing interests.

Received: October 20, 2020
Revised: March 7, 2021
Accepted: April 28, 2021
Published: May 27, 2021

REFERENCES

Amit, I., Winter, D.R., and Jung, S. (2016). The role of the local environment and epigenetics in shaping macrophage identity and their effect on tissue homeostasis. Nat. Immunol. *17*, 18–25.

Anders, S., Pyl, P.T., and Huber, W. (2015). HTSeq–a Python framework to work with high-throughput sequencing data. Bioinformatics *31*, 166–169.

Blackburn, S.D., Shin, H., Haining, W.N., Zou, T., Workman, C.J., Polley, A., Betts, M.R., Freeman, G.J., Vignali, D.A., and Wherry, E.J. (2009). Coregulation of CD8+ T cell exhaustion by multiple inhibitory receptors during chronic viral infection. Nat. Immunol. *10*, 29–37.

Broz, M.L., Binnewies, M., Boldajipour, B., Nelson, A.E., Pollack, J.L., Erle, D.J., Barczak, A., Rosenblum, M.D., Daud, A., Barber, D.L., et al. (2014). Dissecting the tumor myeloid compartment reveals rare activating antigen-presenting cells critical for T cell immunity. Cancer Cell *26*, 638–652.

Butler, A., Hoffman, P., Smibert, P., Papalexi, E., and Satija, R. (2018). Integrating single-cell transcriptomic data across different conditions, technologies, and species. Nat. Biotechnol. *36*, 411–420.

Cassetta, L., Fragkogianni, S., Sims, A.H., Swierczak, A., Forrester, L.M., Zhang, H., Soong, D.Y.H., Cotechini, T., Anur, P., Lin, E.Y., et al. (2019). Human tumor-associated macrophage and monocyte transcriptional landscapes reveal cancer-specific reprogramming, biomarkers, and therapeutic targets. Cancer Cell *35*, 588–602 e510.

Chang, G., Shi, L., Ye, Y., Shi, H., Zeng, L., Tiwary, S., Huse, J.T., Huo, L., Ma, L., Ma, Y., et al. (2020). YTHDF3 induces the translation of m(6)A-enriched gene transcripts to promote breast cancer brain metastasis. Cancer Cell *38*, 857–871 e857.

Cohen, M., Giladi, A., Gorki, A.D., Solodkin, D.G., Zada, M., Hladik, A., Miklosi, A., Salame, T.M., Halpern, K.B., David, E., et al. (2018). Lung single-cell signaling interaction map reveals basophil role in macrophage imprinting. Cell *175*, 1031–1044 e1018.

Coifman, R.R., Lafon, S., Lee, A.B., Maggioni, M., Nadler, B., Warner, F., and Zucker, S.W. (2005). Geometric diffusions as a tool for harmonic analysis and structure definition of data: diffusion maps. Proc. Natl. Acad. Sci. U S A *102*, 7426–7431.

Cui, X., Wei, Z., Zhang, L., Liu, H., Sun, L., Zhang, S.W., Huang, Y., and Meng, J. (2016). Guitar: an R/bioconductor package for gene annotation guided transcriptomic analysis of RNA-related genomic features. Biomed. Res. Int. *2016*, 8367534.

Das, H., Kumar, A., Lin, Z., Patino, W.D., Hwang, P.M., Feinberg, M.W., Majumder, P.K., and Jain, M.K. (2006). Kruppel-like factor 2 (KLF2) regulates proinflammatory activation of monocytes. Proc. Natl. Acad. Sci. U S A *103*, 6653–6658.

DeNardo, D.G., and Ruffell, B. (2019). Macrophages as regulators of tumour immunity and immunotherapy. Nat. Rev. Immunol. *19*, 369–382.

Dobin, A., Davis, C.A., Schlesinger, F., Drenkow, J., Zaleski, C., Jha, S., Batut, P., Chaisson, M., and Gingeras, T.R. (2013). STAR: ultrafast universal RNA-seq aligner. Bioinformatics *29*, 15–21.

Efremova, M., Vento-Tormo, M., Teichmann, S.A., and Vento-Tormo, R. (2020). CellPhoneDB: inferring cell-cell communication from combined expression of multi-subunit ligand-receptor complexes. Nat. Protoc. *15*, 1484–1506.

Egen, J.G., Rothfuchs, A.G., Feng, C.G., Winter, N., Sher, A., and Germain, R.N. (2008). Macrophage and T cell dynamics during the development and disintegration of mycobacterial granulomas. Immunity *28*, 271–284.

Farrell, J.A., Wang, Y., Riesenfeld, S.J., Shekhar, K., Regev, A., and Schier, A.F. (2018). Single-cell reconstruction of developmental trajectories during zebrafish embryogenesis. Science *360*, eaar3131.

Garon, E.B., Rizvi, N.A., Hui, R., Leighl, N., Balmanoukian, A.S., Eder, J.P., Patnaik, A., Aggarwal, C., Gubens, M., Horn, L., et al. (2015). Pembrolizumab for the treatment of non-small-cell lung cancer. N. Engl. J. Med. *372*, 2018–2028.

Guerriero, J.L., Sotayo, A., Ponichtera, H.E., Castrillon, J.A., Pourzia, A.L., Schad, S., Johnson, S.F., Carrasco, R.D., Lazo, S., Bronson, R.T., et al. (2017). Class IIa HDAC inhibition reduces breast tumours and metastases through anti-tumour macrophages. Nature *543*, 428–432.

Haghverdi, L., Buettner, F., and Theis, F.J. (2015). Diffusion maps for high-dimensional single-cell analysis of differentiation data. Bioinformatics *31*, 2989–2998.

Han, D., Liu, J., Chen, C., Dong, L., Liu, Y., Chang, R., Huang, X., Liu, Y., Wang, J., Dougherty, U., et al. (2019). Anti-tumour immunity controlled through mRNA m(6)A methylation and YTHDF1 in dendritic cells. Nature *566*, 270–274.

Heinz, S., Benner, C., Spann, N., Bertolino, E., Lin, Y.C., Laslo, P., Cheng, J.X., Murre, C., Singh, H., and Glass, C.K. (2010). Simple combinations of lineage-determining transcription factors prime cis-regulatory elements required for macrophage and B cell identities. Mol. Cell *38*, 576–589.

Hsu, P.J., Zhu, Y., Ma, H., Guo, Y., Shi, X., Liu, Y., Qi, M., Lu, Z., Shi, H., Wang, J., et al. (2017). Ythdc2 is an N(6)-methyladenosine binding protein that regulates mammalian spermatogenesis. Cell Res. *27*, 1115–1127.

Huang, H., Weng, H., and Chen, J. (2020). m(6)A modification in coding and non-coding RNAs: roles and therapeutic implications in cancer. Cancer Cell *37*, 270–288.

Huang, Y., Su, R., Sheng, Y., Dong, L., Dong, Z., Xu, H., Ni, T., Zhang, Z.S., Zhang, T., Li, C., et al. (2019). Small-molecule targeting of oncogenic FTO demethylase in acute myeloid leukemia. Cancer Cell *35*, 677–691 e610.

Jaitin, D.A., Adlung, L., Thaiss, C.A., Weiner, A., Li, B., Descamps, H., Lundgren, P., Bleriot, C., Liu, Z., Deczkowska, A., et al. (2019). Lipid-associated macrophages control metabolic homeostasis in a Trem2-dependent manner. Cell *178*, 686–698 e614.

Jerby-Arnon, L., Shah, P., Cuoco, M.S., Rodman, C., Su, M.J., Melms, J.C., Leeson, R., Kanodia, A., Mei, S., Lin, J.R., et al. (2018). A cancer cell program promotes T cell exclusion and resistance to checkpoint blockade. Cell *175*, 984–997 e924.

Jia, G., Fu, Y., Zhao, X., Dai, Q., Zheng, G., Yang, Y., Yi, C., Lindahl, T., Pan, T., Yang, Y.G., and He, C. (2011). N6-methyladenosine in nuclear RNA is a major substrate of the obesity-associated FTO. Nat. Chem. Biol. *7*, 885–887.

Jiang, P., Gu, S., Pan, D., Fu, J., Sahu, A., Hu, X., Li, Z., Traugh, N., Bu, X., Li, B., et al. (2018). Signatures of T cell dysfunction and exclusion predict cancer immunotherapy response. Nat. Med. *24*, 1550–1558.

Kale, S., Raja, R., Thorat, D., Soundararajan, G., Patil, T.V., and Kundu, G.C. (2014). Osteopontin signaling upregulates cyclooxygenase-2 expression in tumor-associated macrophages leading to enhanced angiogenesis and melanoma growth via alpha9beta1 integrin. Oncogene *33*, 2295–2306.

Khan, O., Giles, J.R., McDonald, S., Manne, S., Ngiow, S.F., Patel, K.P., Werner, M.T., Huang, A.C., Alexander, K.A., Wu, J.E., et al. (2019). TOX transcriptionally and epigenetically programs CD8(+) T cell exhaustion. Nature *571*, 211–218.

Kim, N., Kim, H.K., Lee, K., Hong, Y., Cho, J.H., Choi, J.W., Lee, J.I., Suh, Y.L., Ku, B.M., Eum, H.H., et al. (2020). Single-cell RNA sequencing demonstrates the molecular and cellular reprogramming of metastatic lung adenocarcinoma. Nat. Commun. *11*, 2285.

Kowalczyk, M.S., Tirosh, I., Heckl, D., Rao, T.N., Dixit, A., Haas, B.J., Schneider, R.K., Wagers, A.J., Ebert, B.L., and Regev, A. (2015). Single-cell RNA-seq reveals changes in cell cycle and differentiation programs upon aging of hematopoietic stem cells. Genome Res. *25*, 1860–1872.

Kuchroo, V.K., Anderson, A.C., and Petrovas, C. (2014). Coinhibitory receptors and CD8 T cell exhaustion in chronic infections. Curr. Opin. HIV AIDS *9*, 439–445.

Langmead, B., and Salzberg, S.L. (2012). Fast gapped-read alignment with Bowtie 2. Nat. Methods *9*, 357–359.

Lavin, Y., Kobayashi, S., Leader, A., Amir, E.D., Elefant, N., Bigenwald, C., Remark, R., Sweeney, R., Becker, C.D., Levine, J.H., et al. (2017). Innate immune landscape in early lung adenocarcinoma by paired single-cell analyses. Cell *169*, 750–765 e717.

Lee, C.W., Ren, Y.J., Marella, M., Wang, M., Hartke, J., and Couto, S.S. (2020). Multiplex immunofluorescence staining and image analysis assay for diffuse large B cell lymphoma. J. Immunol. Methods *478*, 112714.

Lee, H., Bao, S., Qian, Y., Geula, S., Leslie, J., Zhang, C., Hanna, J.H., and Ding, L. (2019). Stage-specific requirement for Mettl3-dependent m(6)A mRNA methylation during haematopoietic stem cell differentiation. Nat. Cell Biol. *21*, 700–709.

Li, H., Handsaker, B., Wysoker, A., Fennell, T., Ruan, J., Homer, N., Marth, G., Abecasis, G., Durbin, R., and Genome Project Data Processing, S. (2009). The sequence alignment/map format and SAMtools. Bioinformatics *25*, 2078–2079.

Liao, X., Sharma, N., Kapadia, F., Zhou, G., Lu, Y., Hong, H., Paruchuri, K., Mahabeleshwar, G.H., Dalmas, E., Venteclef, N., et al. (2011). Kruppel-like factor 4 regulates macrophage polarization. J. Clin. Invest. *121*, 2736–2749.

Liao, Y., Smyth, G.K., and Shi, W. (2019). The R package Rsubread is easier, faster, cheaper and better for alignment and quantification of RNA sequencing reads. Nucleic Acids Res. *47*, e47.

Liu, J., Yue, Y., Han, D., Wang, X., Fu, Y., Zhang, L., Jia, G., Yu, M., Lu, Z., Deng, X., et al. (2014). A METTL3-METTL14 complex mediates mammalian nuclear RNA N6-adenosine methylation. Nat. Chem. Biol. *10*, 93–95.

Liu, N., Dai, Q., Zheng, G., He, C., Parisien, M., and Pan, T. (2015). N(6)-methyladenosine-dependent RNA structural switches regulate RNA-protein interactions. Nature *518*, 560–564.

Locati, M., Curtale, G., and Mantovani, A. (2020). Diversity, mechanisms, and significance of macrophage plasticity. Annu. Rev. Pathol. *15*, 123–147.

Love, M.I., Huber, W., and Anders, S. (2014). Moderated estimation of fold change and dispersion for RNA-seq data with DESeq2. Genome Biol. *15*, 550.

McLane, L.M., Abdel-Hakeem, M.S., and Wherry, E.J. (2019). CD8 T cell exhaustion during chronic viral infection and cancer. Annu. Rev. Immunol. *37*, 457–495.

Meng, J., Cui, X., Rao, M.K., Chen, Y., and Huang, Y. (2013). Exome-based analysis for RNA epigenome sequencing data. Bioinformatics *29*, 1565–1567.

Meng, J., Lu, Z., Liu, H., Zhang, L., Zhang, S., Chen, Y., Rao, M.K., and Huang, Y. (2014). A protocol for RNA methylation differential analysis with MeRIP-Seq data and exomePeak R/Bioconductor package. Methods *69*, 274–281.

Miller, B.C., Sen, D.R., Al Abosy, R., Bi, K., Virkud, Y.V., LaFleur, M.W., Yates, K.B., Lako, A., Felt, K., Naik, G.S., et al. (2019). Subsets of exhausted CD8(+) T cells differentially mediate tumor control and respond to checkpoint blockade. Nat. Immunol. *20*, 326–336.

Nachtergaele, S., and He, C. (2018). Chemical modifications in the life of an mRNA transcript. Annu. Rev. Genet. *52*, 349–372.

Nixon, B.G., Kuo, F., Liu, M., Capistrano, K., Do, M., Franklin, R.A., Wu, X., Kansler, E.R., Srivastava, R.M., Purohit, T.A., et al. (2020). IRF8 Governs Tumor-Associated Macrophage Control of T Cell Exhaustion. bioRxiv. https://doi.org/10.1101/2020.03.12.989731.

Noy, R., and Pollard, J.W. (2014). Tumor-associated macrophages: from mechanisms to therapy. Immunity *41*, 49–61.

Owen, J.L., and Mohamadzadeh, M. (2013). Macrophages and chemokines as mediators of angiogenesis. Front. Physiol. *4*, 159.

Pauken, K.E., Sammons, M.A., Odorizzi, P.M., Manne, S., Godec, J., Khan, O., Drake, A.M., Chen, Z., Sen, D.R., Kurachi, M., et al. (2016). Epigenetic stability of exhausted T cells limits durability of reinvigoration by PD-1 blockade. Science *354*, 1160–1165.

Peranzoni, E., Lemoine, J., Vimeux, L., Feuillet, V., Barrin, S., Kantari-Mimoun, C., Bercovici, N., Guerin, M., Biton, J., Ouakrim, H., et al. (2018). Macrophages impede CD8 T cells from reaching tumor cells and limit the efficacy of anti-PD-1 treatment. Proc. Natl. Acad. Sci. U S A *115*, E4041–E4050.

Philip, M., Fairchild, L., Sun, L., Horste, E.L., Camara, S., Shakiba, M., Scott, A.C., Viale, A., Lauer, P., Merghoub, T., et al. (2017). Chromatin states define tumour-specific T cell dysfunction and reprogramming. Nature *545*, 452–456.

Ping, X.L., Sun, B.F., Wang, L., Xiao, W., Yang, X., Wang, W.J., Adhikari, S., Shi, Y., Lv, Y., Chen, Y.S., et al. (2014). Mammalian WTAP is a regulatory subunit of the RNA N6-methyladenosine methyltransferase. Cell Res. *24*, 177–189.

Powles, T., Eder, J.P., Fine, G.D., Braiteh, F.S., Loriot, Y., Cruz, C., Bellmunt, J., Burris, H.A., Petrylak, D.P., Teng, S.L., et al. (2014). MPDL3280A (anti-PD-L1) treatment leads to clinical activity in metastatic bladder cancer. Nature *515*, 558–562.

Quinlan, A.R., and Hall, I.M. (2010). BEDTools: a flexible suite of utilities for comparing genomic features. Bioinformatics *26*, 841–842.

Ribas, A., and Wolchok, J.D. (2018). Cancer immunotherapy using checkpoint blockade. Science *359*, 1350–1355.

Rodriguez-Ubreva, J., Catala-Moll, F., Obermajer, N., Alvarez-Errico, D., Ramirez, R.N., Company, C., Vento-Tormo, R., Moreno-Bueno, G., Edwards, R.P., Mortazavi, A., et al. (2017). Prostaglandin E2 leads to the acquisition of DNMT3A-dependent tolerogenic functions in human myeloid-derived suppressor cells. Cell Rep. *21*, 154–167.

Ruffell, B., Chang-Strachan, D., Chan, V., Rosenbusch, A., Ho, C.M., Pryer, N., Daniel, D., Hwang, E.S., Rugo, H.S., and Coussens, L.M. (2014). Macrophage IL-10 blocks CD8+ T cell-dependent responses to chemotherapy by suppressing IL-12 expression in intratumoral dendritic cells. Cancer Cell *26*, 623–637.

Sade-Feldman, M., Yizhak, K., Bjorgaard, S.L., Ray, J.P., de Boer, C.G., Jenkins, R.W., Lieb, D.J., Chen, J.H., Frederick, D.T., Barzily-Rokni, M., et al. (2018). Defining T cell states associated with response to checkpoint immunotherapy in melanoma. Cell *175*, 998–1013 e1020.

Sawant, D.V., Yano, H., Chikina, M., Zhang, Q., Liao, M., Liu, C., Callahan, D.J., Sun, Z., Sun, T., Tabib, T., et al. (2019). Adaptive plasticity of IL-10(+) and IL-

35(+) Treg cells cooperatively promotes tumor T cell exhaustion. Nat. Immunol. *20*, 724–735.

Schietinger, A., Philip, M., Krisnawan, V.E., Chiu, E.Y., Delrow, J.J., Basom, R.S., Lauer, P., Brockstedt, D.G., Knoblaugh, S.E., Hammerling, G.J., et al. (2016). Tumor-specific T cell dysfunction is a dynamic antigen-driven differentiation program initiated early during tumorigenesis. Immunity *45*, 389–401.

Schlager, C., Korner, H., Krueger, M., Vidoli, S., Haberl, M., Mielke, D., Brylla, E., Issekutz, T., Cabanas, C., Nelson, P.J., et al. (2016). Effector T-cell trafficking between the leptomeninges and the cerebrospinal fluid. Nature *530*, 349–353.

Sharma, P., and Allison, J.P. (2015). Immune checkpoint targeting in cancer therapy: toward combination strategies with curative potential. Cell *161*, 205–214.

Shi, H., Wang, X., Lu, Z., Zhao, B.S., Ma, H., Hsu, P.J., Liu, C., and He, C. (2017). YTHDF3 facilitates translation and decay of N(6)-methyladenosine-modified RNA. Cell Res. *27*, 315–328.

Speiser, D.E., Ho, P.C., and Verdeil, G. (2016). Regulatory circuits of T cell function in cancer. Nat. Rev. Immunol. *16*, 599–611.

Su, R., Dong, L., Li, Y., Gao, M., Han, L., Wunderlich, M., Deng, X., Li, H., Huang, Y., Gao, L., et al. (2020). Targeting FTO suppresses cancer stem cell maintenance and immune evasion. Cancer Cell *38*, 79–96 e11.

Tang, H., Liang, Y., Anders, R.A., Taube, J.M., Qiu, X., Mulgaonkar, A., Liu, X., Harrington, S.M., Guo, J., Xin, Y., et al. (2018). PD-L1 on host cells is essential for PD-L1 blockade-mediated tumor regression. J. Clin. Invest. *128*, 580–588.

Thommen, D.S., and Schumacher, T.N. (2018). T cell dysfunction in cancer. Cancer Cell *33*, 547–562.

Trapnell, C., Cacchiarelli, D., Grimsby, J., Pokharel, P., Li, S., Morse, M., Lennon, N.J., Livak, K.J., Mikkelsen, T.S., and Rinn, J.L. (2014). The dynamics and regulators of cell fate decisions are revealed by pseudotemporal ordering of single cells. Nat. Biotechnol. *32*, 381–386.

Turnis, M.E., Sawant, D.V., Szymczak-Workman, A.L., Andrews, L.P., Delgoffe, G.M., Yano, H., Beres, A.J., Vogel, P., Workman, C.J., and Vignali, D.A. (2016). Interleukin-35 limits anti-tumor immunity. Immunity *44*, 316–329.

Tzetzo, S.L., and Abrams, S.I. (2021). Redirecting macrophage function to sustain their "defender" antitumor activity. Cancer Cell *S1535-6108*, 00160–00164.

Vento-Tormo, R., Efremova, M., Botting, R.A., Turco, M.Y., Vento-Tormo, M., Meyer, K.B., Park, J.E., Stephenson, E., Polanski, K., Goncalves, A., et al. (2018). Single-cell reconstruction of the early maternal-fetal interface in humans. Nature *563*, 347–353.

Vignali, D.A., and Kuchroo, V.K. (2012). IL-12 family cytokines: immunological playmakers. Nat. Immunol. *13*, 722–728.

Wang, X., Cao, Q., Yu, L., Shi, H., Xue, B., and Shi, H. (2016). Epigenetic regulation of macrophage polarization and inflammation by DNA methylation in obesity. JCI Insight *1*, e87748.

Wang, X., Lu, Z., Gomez, A., Hon, G.C., Yue, Y., Han, D., Fu, Y., Parisien, M., Dai, Q., Jia, G., et al. (2014). N6-methyladenosine-dependent regulation of messenger RNA stability. Nature *505*, 117–120.

Wang, X., Zhao, B.S., Roundtree, I.A., Lu, Z., Han, D., Ma, H., Weng, X., Chen, K., Shi, H., and He, C. (2015). N(6)-methyladenosine modulates messenger RNA translation efficiency. Cell *161*, 1388–1399.

Wei, S.C., Levine, J.H., Cogdill, A.P., Zhao, Y., Anang, N.A.S., Andrews, M.C., Sharma, P., Wang, J., Wargo, J.A., Pe'er, D., and Allison, J.P. (2017). Distinct cellular mechanisms underlie anti-CTLA-4 and anti-PD-1 checkpoint blockade. Cell *170*, 1120–1133.e17.

Wherry, E.J., Ha, S.J., Kaech, S.M., Haining, W.N., Sarkar, S., Kalia, V., Subramaniam, S., Blattman, J.N., Barber, D.L., and Ahmed, R. (2007). Molecular signature of CD8+ T cell exhaustion during chronic viral infection. Immunity *27*, 670–684.

Wolf, F.A., Angerer, P., and Theis, F.J. (2018). SCANPY: large-scale single-cell gene expression data analysis. Genome Biol. *19*, 15.

Xia, A., Zhang, Y., Xu, J., Yin, T., and Lu, X.J. (2019). T cell dysfunction in cancer immunity and immunotherapy. Front. Immunol. *10*, 1719.

Yang, X., Yang, Y., Sun, B.F., Chen, Y.S., Xu, J.W., Lai, W.Y., Li, A., Wang, X., Bhattarai, D.P., Xiao, W., et al. (2017). 5-methylcytosine promotes mRNA export - NSUN2 as the methyltransferase and ALYREF as an m(5)C reader. Cell Res. *27*, 606–625.

Zhang, L., Li, Z., Skrzypczynska, K.M., Fang, Q., Zhang, W., O'Brien, S.A., He, Y., Wang, L., Zhang, Q., Kim, A., et al. (2020). Single-cell analyses inform mechanisms of myeloid-targeted therapies in colon cancer. Cell *181*, 442–459 e429.

Zhang, Q., He, Y., Luo, N., Patel, S.J., Han, Y., Gao, R., Modak, M., Carotta, S., Haslinger, C., Kind, D., et al. (2019). Landscape and dynamics of single immune cells in hepatocellular carcinoma. Cell *179*, 829–845.e20.

Zheng, G., Dahl, J.A., Niu, Y., Fedorcsak, P., Huang, C.M., Li, C.J., Vagbo, C.B., Shi, Y., Wang, W.L., Song, S.H., et al. (2013). ALKBH5 is a mammalian RNA demethylase that impacts RNA metabolism and mouse fertility. Mol. Cell *49*, 18–29.

Please cite this article in press as: Dong et al., The loss of RNA N^6-adenosine methyltransferase *Mettl14* in tumor-associated macrophages promotes $CD8^+$ T cell dysfunction and tumor growth, Cancer Cell (2021), https://doi.org/10.1016/j.ccell.2021.04.016

STAR★METHODS

KEY RESOURCES TABLE

REAGENT or RESOURCE	SOURCE	IDENTIFIER
Antibodies		
Anti-CD4	BioLegend	Cat#100414; RRID: AB_312699
Anti-CD8a	BioLegend	Cat#100712; RRID: AB_312751
Anti-CD11b	BioLegend	Cat#101228; RRID: AB_893232
Anti-CD11c	BioLegend	Cat#117318; RRID: AB_493568
Anti-Ly6G	BioLegend	Cat# 127621; RRID:AB_10640452
Anti-CD24	BioLegend	Cat#101831; RRID: AB_2563894
Anti-CD45	BioLegend	Cat#103138; RRID: AB_2563061
Anti-IA/IE	BioLegend	Cat# 107622; RRID:AB_493727
Anti-F4/80	BioLegend	Cat# 123116; RRID:AB_893481
Anti-C1q	Thermo Fisher Scientific	Cat# MA1-40312; RRID:AB_2067274
Anti-MERTK	Thermo Fisher Scientific	Cat# 25-5751-82; RRID:AB_2573466
Anti-CX3CR1	BioLegend	Cat# 149005; RRID:AB_2564314
Anti-CD44	BioLegend	Cat# 103006; RRID:AB_312957
Anti-PD-1	BioLegend	Cat# 135231; RRID:AB_2566158
Anti-LAG-3	BioLegend	Cat# 125221; RRID:AB_2572080
Anti-TIM-3	BioLegend	Cat# 119717; RRID:AB_2571934
Anti-CD62L	BioLegend	Cat# 104437; RRID:AB_11125577
Anti-TIGIT	Thermo Fisher Scientific	Cat# 12-9501-80; RRID:AB_11039537
Anti-TOX	Thermo Fisher Scientific	Cat# 12-6502-82; RRID:AB_10855034
Anti-CD39	Thermo Fisher Scientific	Cat# 25-0391-82; RRID:AB_1210766
Anti-CD86	BioLegend	Cat# 105029; RRID:AB_2074993
Anti-PD-L1	BioLegend	Cat# 124319; RRID:AB_2563619
Anti-Ly6C	BioLegend	Cat# 128006; RRID:AB_1186135
Anti-CD103	BioLegend	Cat# 121413; RRID:AB_1227503
Anti-Ki-67	Thermo Fisher Scientific	Cat# 17-5698-82, RRID:AB_2688057
Anti-BCL-2	BD Biosciences	Cat# 554221; RRID:AB_395312
Anti-EBI3	R and D Systems	Cat# IC18341A; RRID:AB_10890620
Anti-FLAG	TransGen biotech	Cat#HT201-01
Anti-METTL14	Abcam	Cat#ab98166; RRID:AB_10672570
Anti-METTL14	Abcam	Cat#ab220030 Clone: CL4252
Anti-METTL3	Abcam	Cat# ab195352; RRID:AB_2721254
Anti-YTHDF2	Abcam	Cat# ab220163; RRID:AB_2868573
Goat anti-Rabbit IgG (H+L) Cross-Adsorbed Secondary Antibody, Alexa Fluor 647	Thermo Fisher Scientific	Cat# A-21244; RRID:AB_2535812
Brilliant Violet 421(TM) Goat anti-mouse IgG (minimal x-reactivity) antibody	BioLegend	Cat# 405317; RRID:AB_10900419

(*Continued on next page*)

Please cite this article in press as: Dong et al., The loss of RNA N^6-adenosine methyltransferase *Mettl14* in tumor-associated macrophages promotes $CD8^+$ T cell dysfunction and tumor growth, Cancer Cell (2021), https://doi.org/10.1016/j.ccell.2021.04.016

Continued

REAGENT or RESOURCE	SOURCE	IDENTIFIER
Fc Block	Bio X Cell	Cat# BE0307; RRID:AB_2736987
Anti-ARG1	Thermo Fisher Scientific	Cat# 17-3697-80; RRID:AB_2734834
Anti-CD206	BioLegend	Cat# 141706; RRID:AB_10895754
Anti-CD64	BioLegend	Cat# 139323; RRID:AB_2629778
Anti-B220	BioLegend	Cat# 103206; RRID:AB_312991
Anti-Granzyme B	BioLegend	Cat#372206; RRID: AB_2687030
Anti-H-$2K^b$	BioLegend	Cat#116513; RRID: AB_1967103
Anti-IFNγ	BioLegend	Cat#505808; RRID: AB_315402
m^6A antibody	abcam	Cat#ab151230; RRID: AB_2753144
EBI3 neutralizing antibody	Emdmillipore	Cat#MABF848; clone: V1.4C4.22
Anti-CD68	Abcam	Cat#ab955; RRID:AB_307338
Anti-CD68	Abcam	Cat# ab213363; RRID:AB_2801637
Anti-EBI3 (Human)	Abcam	Cat#ab272709
CD8 depletion antibody	BioLegend	clone YTS169.4
Anti-IFNγ for ELISPOT	BD Bioscience	Cat# 554408; RRID:AB_395373
Biotinylated anti-IFNγ antibody	BioLegend	Cat# 505804; RRID:AB_315398
Anti-CD8 (Human)	Abcam	Cat# ab17147; RRID:AB_443686
Biological Samples		
Colorectal cancer specimen for IHC	University of Chicago	See Table S5 for details
Colorectal cancer specimen for Multi-color Immunohistochemistry (IHC)	Peking University Cancer Hospital & Institute.	See Table S5 for details
Chemicals, peptides, and recombinant proteins		
Brefeldin A	Thermo Fisher	Cat#00-4506-51
Collagenase IV	Sigma-Aldrich	Cat#C4-22-1G
DAPI	Life technology	Cat#D1306
DNase I	Roche	Cat#10104159001
Fetal bovine serum	Gemini	Cat#900-108
HEPES	Thermo Fisher	Cat#15630080
IL-2	PEPROTECH	Cat#589104
L-glutamine	Thermo Fisher	Cat#25030081
Non-essential amino acids	Thermo Fisher	Cat#11140050
TRIzol reagent	Invitrogen	Cat#15596018
Human IL-35	PEPROTECH	Cat# 200-37-10UG
PMA	Sigma	Cat# P1585-1MG
Ionomycin	Sigma	Cat# I0634-1MG
M-CSF carrier-free	BioLegend	Cat# 576406
Liberase TL	Roche	Cat#5401020001
OT-I peptide (SIINFEKL)	Beijing Scilight Biotechnology LLC.	N/A
Avidin-horseradish peroxidase	BD Bioscience	Cat#00-4100-94
Trypan Blue	Gibco	Cat#15250061
Critical commercial assays		
RNA Fragmentation Reagents	Invitrogen	Cat#AM8740
EpiMark N6-Methyladenosine enrichment kit	NEB	Cat#E1610S
Dynabeads™ mRNA direct™ purification kit	Thermo Fisher Scientific	Cat#61002
TIANamp N96 genomic DNA kit	TIANGEN	Cat#DP314-T
2 × Taq Master Mix, Dye Plus	Vazyme Biotech	Cat#P112-03,

(*Continued on next page*)

Continued

REAGENT or RESOURCE	SOURCE	IDENTIFIER
Fixation Buffer	BioLegend	Cat# 420801
Intracellular Staining Permeabilization Wash Buffer (10×)	BioLegend	Cat#420801
Foxp3/Transcription Factor Staining Buffer Set	Invitrogen	Cat#00-5523-00
IFNγ Flex Set CBA Kit	BD Bioscience	Cat#558296
Cytometric Bead Array Mouse Inflammation Kit	BD Bioscience	Cat#552364
DNA Clean & Concentration-5	ZYMO RESEARCH	Cat#D4014
TransStart Top Green qPCR SuperMix	TansGen	Cat#AQ101
PrimeScript RT reagent Kit	Takara	Cat#RR037A
PowerUp SYBR Green Master Mix	Thermo Fisher	Cat#A25741
FastStart Essential DNA Green Master	Roche	Cat#4673484001
VECTASTAIN Elite ABC HRP Kit and DAB Substrate Kit	Vector Laboratories	Cat#PK-6100
Opal 7-Color Manual IHC kit	AKOYA BIOSCIENCES	Cat#NEL811001KT
IHC Antigen Retrieval Solution 10× High pH	Invitrogen	Cat#00-4956-58
IHC Antigen Retrieval Solution 10 Low pH	Invitrogen	Cat#00-4956-58
Chromium Next GEM Single Cell 3′ GEM, Library & Gel Bead Kit v3.1	10X Genomics	Cat#1000128
Deposited data		
Data files for mouse RNA-seq	This paper	GEO: GSE155098
Data files for mouse m^6A-seq	This paper	GEO: GSE155098
Data files for mouse scRNA-seq	This paper	GEO: GSE155098
Data files for human colorectal cancer RNA-seq	This paper	GEO: GSE155098
Human melanoma scRNA-seq	(Sade-Feldman et al., 2018)	GEO: GSE120575
Human non-small cell lung cancer scRNA-seq	(Kim et al., 2020)	GEO: GSE131907
Human LUAD TCGA dataset	N/A	https://www.cancer.gov/about-nci/organization/ccg/research/structural-genomics/tcga
Experimental models: cell lines		
LLC	ATCC	CRL-1642
MC38	(Deng et al., 2014)	N/A
B16-OZ	(Han et al., 2019)	N/A
B16-OVA	(Han et al., 2019)	N/A
B16F10	ATCC	CRL-6475
Experimental models: organisms/strains		
C57BL/6 mice	Charles River Laboratories	N/A
LysM^{Cre} mice	The Jackson Laboratory	N/A
Mettl14$^{flox/flox}$ mice	Shanghai Model Organisms Center, Inc	N/A
Mettl3$^{flox/flox}$ mice	Shanghai Model Organisms Center, Inc	N/A
Ythdf2 KI mice	GemPharmatech Co., Ltd	N/A
MafB^{cre} mice	The Jackson Laboratory	N/A
Ythdf2$^{flox/flox}$ mice	Bin Shen, (Li et al., 2018)	N/A
Oligonucleotides		
5′-AUUGUCA(m^6A)CAGCAGC-3′	Genescript, China	N/A
5′-ATTGCCATTCTCGATAGG(dm^6A) TCCGGTCAAACCTAGACGAA-3′	Generay, China	N/A

(*Continued on next page*)

Please cite this article in press as: Dong et al., The loss of RNA N^6-adenosine methyltransferase *Mettl14* in tumor-associated macrophages promotes $CD8^+$ T cell dysfunction and tumor growth, Cancer Cell (2021), https://doi.org/10.1016/j.ccell.2021.04.016

Continued

REAGENT or RESOURCE	SOURCE	IDENTIFIER
Software and algorithms		
Cell Ranger v3.0.2	10X Genomics	https://support.10xgenomics.com/single-cell-gene-expression/software/pipelines/latest/installation
InForm Advanced Image Analysis Software (PerkinElmer)	(Lee et al., 2020)	https://www.akoyabio.com/support/software/#inform_tissue_analysis_software
Seurat R package v3.1.4	(Butler et al., 2018)	https://github.com/satijalab/seurat/releases
CellPhoneDB	(Efremova et al., 2020; Vento-Tormo et al., 2018)	https://github.com/Teichlab/cellphonedb
URD R package v1.1.1	(Farrell et al., 2018)	https://github.com/farrellja/URD
scanpy toolkit	(Wolf et al., 2018)	https://github.com/theislab/scanpy
Trim Galore! v0.6.0	N/A	http://www.bioinformatics.babraham.ac.uk/projects/trim_galore
Bowtie2 v2.3.5	(Langmead and Salzberg, 2012)	http://bowtie-bio.sourceforge.net/bowtie2/index.shtml
STAR v2.7.0f	(Dobin et al., 2013)	https://github.com/alexdobin/STAR
SAMtools v1.9	(Li et al., 2009)	http://www.htslib.org/download/
Rsubread R package v2.0.1	(Liao et al., 2019)	https://bioconductor.org/packages/release/bioc/html/Rsubread.html
DESeq2 R pakage v1.26.0	(Love et al., 2014)	https://bioconductor.org/packages/release/bioc/html/DESeq2.html
HTSeq	(Anders et al., 2015)	https://htseq.readthedocs.io/en/master/
exomePeak R package v2.16.0	(Meng et al., 2014)	https://www.bioconductor.org/packages/3.8/bioc/html/exomePeak.html
Bedtools v2.28.0	(Quinlan and Hall, 2010)	https://github.com/arq5x/bedtools2/releases/tag/v2.28.0
HOMER v4.10.4	(Heinz et al., 2010)	http://homer.ucsd.edu/homer/
GUITAR R package v1.14.0	(Cui et al., 2016)	https://bioconductor.statistik.tu-dortmund.de/packages/3.5/bioc/html/Guitar.html
Monocle R package v2.14.0	(Trapnell et al., 2014)	http://cole-trapnell-lab.github.io/monocle-release/

RESOURCE AVAILABILITY

Lead contact

Further information and requests for resources and reagents should be directed to and will be fulfilled by the Lead Contact, Dali Han (handl@big.ac.cn).

Materials availability

This study did not generate new unique reagents.

Data and code availability

The accession number for the raw sequencing data and processed data reported in this paper is: GEO: GSE155098. The single-cell RNA sequencing datasets from melanoma (Sade-Feldman et al., 2018) and non-small cell lung cancer (Kim et al., 2020) were available from GEO: GSE120575 and GEO: GSE131907, respectively.

EXPERIMENTAL MODEL AND SUBJECT DETAILS

Mice

Mettl14$^{flox/flox}$ mice were kindly provided by Professor Chuan He (University of Chicago). *Mettl3*$^{flox/flox}$ mice were kindly provided by Professor Qingfeng Wu (Institute of Genetics and Developmental Biology, Chinese Academy of Sciences). *Ythdf2*$^{flox/flox}$ mice were kindly provided by Professor Bin Shen (Nanjing Medical University). *LysM*^{Cre} mice were purchased from The Jackson Laboratory. All

Please cite this article in press as: Dong et al., The loss of RNA N^6-adenosine methyltransferase *Mettl14* in tumor-associated macrophages promotes $CD8^+$ T cell dysfunction and tumor growth, Cancer Cell (2021), https://doi.org/10.1016/j.ccell.2021.04.016

mice are maintained under pathogen-free conditions. Mice with 6–12 weeks of age were used for all animal experiments. All mice were used in accordance with Tsinghua University Animal Ethics Committee guidelines.

Cell line

As previously described (Han et al., 2019), B16-OVA is a clone derived from the mouse melanoma cell line B16-F10 (ATCC, CRL-6475) transfected with OVA. B16-F10-zsGreen-OTIp (B16-OZ) is a single clone that is selected after being transduced by lentivirus expressing zsGreen-OTIp (SIINFEKL). LLC (ATCC, CRL-1642) is a Lewis lung carcinoma cell line, and MC38 is a mouse colon adenocarcinoma cell line as previously described (Han et al., 2019). Cells were cultured in Dulbecco's modified Eagle's medium (DMEM; Invitrogen) containing 10% heat-inactivated fetal bovine serum (FBS, Gemini), 2 mM L-glutamine (Thermo Fisher), 10 mM HEPES (Thermo Fisher), and 0.1 mM non-essential amino acids (NEAA, Thermo Fisher). All cells were cultured at 37°C in 5% CO_2.

Ythdf2-3×Flag-GGS-Avi-GGS knock-in mouse lineage establishment

Generation of CRISPR/Cas9-mediated knock-in mice was done at GemPharmatech Co., Ltd. All the procedures were done in GemPharmatech Co., Ltd until the birth of whole knock-in litters. Homologous arm surrounding *Ythdf2* gene start codon was amplified from genome DNA and cloned to construction vector, and then synthesized 3×Flag-GGS-Avi-GGS fragment was inserted just following start codon by recombination. After Cas9/gRNA-mediated double-strand break, this donor could be used as a template to introduce homologous recombination repair. gRNA 5'-TGAGGATCCGAGAGCCATGT-3'' was cloned to gRNA scaffold and then transcribed *in vitro*. Donor, gRNA and Cas9 were co-injected into the C57BL6/J zygotes. Operated zygotes were introduced into pseudopregnant host females and carried to term. Born mice were identified, and the mice with 3×Flag-GGS-Avi-GGS knock-in were used as founders to be crossed with C57BL6/J to ensure germline transmission and eliminate any possible mosaicism. Heterozygous mice were then mated to generate homozygous offspring.

Human specimens

Fresh tumor and adjacent normal tissue samples of 22 colorectal cancer patients were surgically resected and obtained with informed consent under a protocol approved by the University of Chicago Institutional Review Board. We complied with all relevant ethical regulations. For the Multi-color IHC staining, the sample from the colon cancer patient was surgically resected and obtained with informed consent under a protocol approved by Beijing Cancer Hospital ethics committee. Information about the sex, age, and tumor characteristics of patients is provided in Table S5.

METHOD DETAILS

Mouse genotyping

For genotyping of *Ythdf2*-3×Flag-GGS-Avi-GGS knock-in mouse, DNA was extracted from mice tails by TIANamp N96 genomic DNA kit (Cat: DP314-T, TIANGEN Co., Ltd, Beijing, China). PCR program for genotyping was set as 20 cycles of 65°C, decreasing 0.5°C per cycle and 20 cycles of 55°C for annealing. Genotype reactions were performed using 2 × Taq Master Mix, Dye Plus (Cat: P112-03, Vazyme Biotech Co., Ltd, Nanjing, China). Three pairs of primers were used to do genotype PCR with possible founder mice. Primer forward 1: 5'-TGACACTGTGCATACGGGTGAG-3' and primer reverse 1: 5'-CACCCTCGTGCCACTCGATT-3' could amplify 5' arm and produce a band with 1,088 bp for inserted allele but no band for wild-type one. Primer forward 2: 5'-CATGGACTACAAGGACCACGAC-3' and primer reverse 2: 5'-GGAATAACGATGAGCGCCAG-3' could amplify 3' arm and produce a band with 1,096 bp for inserted allele but no band for wild-type one. Primer forward 3: 5'-ATAGAGACGGGCGTTGAGCTC-3' and primer reverse 3: 5'- CACACAATGGCCGAGACATG-3' could produce bands with 415 and 286 bp for wild-type one.

Tumor growth and treatment

5×10^5 B16-OZ, B16-OVA, MC38, LLC or 10^5 B16F10 tumor cells were implanted subcutaneously (s.c.) into the flank of mice. The length (a) and width (b) of the tumors were measured starting at day 7 and every two days thereafter, and tumor volume was calculated with formula $(ab^2)/2$. For EBI3 blockade *in vivo*, mice were injected with 5×10^5 B16-OZ cells. Tumor-bearing WT and *Mettl14*-cKO mice were treated with 4 μg EBI3 neutralizing antibody (Emdmillipore, clone: V1.4C4.22) intratumorally on days 8 and 10. The tumor volume of the EBI3 treatment group was measured together with control groups.

To deplete $CD8^+$ T cells *in vivo*, 200 μg of anti-CD8 antibody (clone YTS169.4) was injected intraperitoneally (i.p.) to WT and *Mettl14* cKO mice on days -2 and 3 upon tumor inoculation. For the study of neutralizing EBI3 and depleting $CD8^+$ T cells, WT and *Mettl14* cKO mice were injected subcutaneously with 5×10^5 B16-OZ cells. Tumor-bearing mice were intratumorally injected with anti-EBI3 neutralizing antibody (4 μg) and 200 μg of CD8 depleting antibody on days 8 and 10. The tumor volume was monitored over time.

Flow cytometry and cell sorting

For single cell suspension preparation, collected tumors were digested with 0.26 U/ml Liberase TL (B16-OZ) or 1 mg/ml Collagenase IV (LLC) and 0.25 mg/ml DNase I at 37°C for 30 min and filtered through a 70 μm cell strainer. Cells were washed twice with staining buffer (PBS supplemented with 2% FBS and 1 mM EDTA), and then resuspended in staining buffer and incubated with Fc Block (clone 2.4G2; BioX Cell) for 10 min. Subsequently, indicated antibodies were added, and staining was continued for 30 min on ice in the dark. For the composition of TME determination, $CD45^+Ly6C^-CD11b^+F4/80^+$ macrophages, $Ly6C^+CD11b^+$ monocytes,

Please cite this article in press as: Dong et al., The loss of RNA N^6-adenosine methyltransferase *Mettl14* in tumor-associated macrophages promotes $CD8^+$ T cell dysfunction and tumor growth, Cancer Cell (2021), https://doi.org/10.1016/j.ccell.2021.04.016

$Ly6C^-CD11b^+F4/80^-CD24^+$ dendritic cells, $CD4^+$ and $CD8^+$ T cells were analyzed by flow cytometry. Data were collected on an LSR II cytometer (BD) after a washing step and analyzed with FlowJo software (TreeStar). Where applicable, cell sorting was conducted with AriaIII (BD) after specific antibody incubation.

For intracellular staining of METTL14 in $CX3CR1^+MHCII^+$ and $CX3CR1^-MHCII^-$ macrophages, cells were fixed with Fixation/Permeabilization Concentrate (Invitrogen) and Fixation/Perm Diluent (Invitrogen) at a ratio of 1:3 for 30 min at 4°C, and then washed twice with diluted 1 × Permeabilization Buffer (10 ×, BioLegend). Antibodies against METTL14 (Abcam, ab98166) was added and incubated at 4°C overnight, followed by adding the Alexa Flour 647 goat anti-rabbit IgG (Life technologies) and staining for 1 hr. For knockout efficacy validation of METTL14 and METTL3, after the surface staining step, cells were fixed with Fixation Buffer (BioLegend) for 20 min at 4°C and permeabilized with 0.5% Triton X-100. Antibody against METTL14 (Abcam, ab220030) and METTL3 (Abcam, ab195352) were used for the staining.

For intracellular staining of YTHDF2, tumor-infiltrating cells from *Ythdf2* KI and B6 mice on day 15 were performed surface staining and fixed with Fixation Buffer (BioLegend) for 20 min at 4°C, and then washed twice with diluted 1 × Permeabilization Buffer (10 ×, BioLegend). Antibody against DYKDDDDK Tag (Flag) was added and incubated at 4°C for 1 hr followed by washing with Permeabilization Buffer prior to flow cytometric analysis. For knockout efficacy validation of YTHDF2, antibody against YTHDF2 (Abcam, ab220163) were added and incubated at 4°C overnight, followed by adding the Alexa Flour 647 goat anti-rabbit IgG (Life technologies) and staining for 1 hr.

TOX and Ki-67 staining was conducted following the manufacturer's instructions of the Foxp3/Transcription Factor Staining Buffer Set (Invitrogen).

Cytokine detection of tumor-infiltrating T cells

Tumor-infiltrating leukocytes were stimulated with 2.5 μg/ml phorbol-12-myristate-13-acetate (PMA) and 0.5 μg/ml ionomycin and blocked with 1 × Bredeldin A (BioLegend) simultaneously for 4 hr at 37°C in 5% CO_2. After a washing step, cells were stained with anti-CD45 and anti-CD8. For intracellular staining, cells were fixed with the Fixation Buffer (BioLegend) for 20 min and then washed twice with diluted 1 × Permeabilization Buffer (10 ×, BioLegend). Antibodies against IFNγ and GZMB were added and incubated at 4°C for 1 hr followed by washing with Permeabilization Buffer prior to flow cytometric analysis.

Co-culture assay for macrophages and T cells

To detect the immunosuppressive effect of macrophages to $CD8^+$ T cells, $C1q^+$ TAMs and $PTGS2^+$ TAMs were isolated from day 14 B16-OZ bearing WT and *Mettl14* cKO mice, followed by co-cultured with OT-I T cells that was stimulated with 1 μg/ml OT-I peptide (SIINFEKL, synthesized by Beijing Scilight Biotechnology LLC.) for 72 hr. The immunosuppressive effect of macrophages to $CD8^+$ T cells was evaluated by IFNγ production of $CD8^+$ T cells.

In vitro T cells and macrophages treatment

For the assay to detect whether IL-35 acts directly to $CD8^+$ T cells, OT-I T cells were stimulated with 0.5 ng/μl OT-I peptide in the presence or absence of 25 ng/ml IL-35 for 72 hr. T cell function was evaluated by IFNγ production using IFNγ Flex Set CBA Kit (BD). To detect whether IL-35 alters macrophage in producing inflammatory cytokines, $C1q^+$ TAMs were isolated from day 14 B16-OVA tumor-bearing WT mice and treated with IL-35 overnight. The production of inflammatory cytokines by macrophages was detected using the Cytometric Bead Array Mouse Inflammation Kit (BD) according to the manufacturer's instructions. To detect whether macrophages response to IFNγ, $C1q^+$ TAMs and $PTGS2^+$ TAMs were isolated from WT and *Mettl14* cKO day14 B16-OZ bearing mice and then treated with 10 ng/ml IFNγ for 16 h. MHCI, MHCII, CD86, and PD-L1 expression of macrophages were detected by flow cytometry.

Measurement of IFNγ-secreting $CD8^+$ T cells by ELISPOT assay

For antigen-specific $CD8^+$ T cell functional assay in the MC38 model, fourteen days after tumor inoculation, 5×10^5 lymphocytes were re-stimulated with 10^4 MC38 tumor cells (lymphocyte:MC38 = 50:1) for 72 hr. A 96-well HTS-IP plate (Millipore) was pre-coated with anti-IFNγ antibody (BD) with a 1:250 dilution overnight at 4°C. After co-culture, cells were removed. Biotinylated anti-IFNγ antibody (BioLegend) with a 1:250 dilution was added and incubated for 2 hr at room temperature. Avidin-horseradish peroxidase (BD) with a 1:1,000 dilution was then added and the plate was incubated for 1 hr at room temperature. IFNγ spots were developed according to the manufacturer' s instructions (BD).

Orthotopic lung tumor model induction and tissue processing

4×10^5 LLC tumor cells were injected intravenously to WT and *Mettl14* cKO mice. 12 days post tumor cells injection, WT and *Mettl14* cKO mice were sacrificed and the lungs were collected. Samples were digested with 0.26 U/ml LiberaseTL (Roche) and 0.25 mg/ml DNaseI (Roche) in 1 ml of DMEM (GIBCO) in C-Tubes (Miltenyi) and briefly processed with a GentleMACS Dissociator (Miltenyi), followed by being incubated at 37°C for 30 min and processed a second time via GentleMACS. Single-cell suspension was then obtained by filtering the cells through a 70 μm cell strainer.

Bone marrow-derived macrophage induction

Single-cell suspension of BMMs was cultured in DMEM medium containing 10% FBS and 20 ng/ml Recombinant Mouse M-CSF carrier-free (BioLegend) in a 6-well plate at a concentration of 2×10^6 /ml. Fresh medium supplemented with M-CSF was added on days 3, 5, and 7 to induce bone marrow-derived macrophage. On day 7, macrophages were collected to perform UHPLC-MRM-MS/MS analysis or m^6A-seq.

DNA/RNA extraction and qPCR analysis for gene expression

To detect the knockout efficacy *in vivo*, $Ly6C^-CD11b^+F4/80^+$ macrophages, $Ly6C^+CD11b^+$ monocytes and $Ly6C^{int}CD11b^+$ neutrophils from the spleens of naive WT and *Mettl14* cKO mice were sorted based on flow cytometry. Genomic DNA was isolated with DNA Clean & Concentration-5 (ZYMO RESEARCH) following the manufacturer's protocol. Purified DNA samples were then performed qPCR with TransStart Top Green qPCR SuperMix (TansGen) in a StepOne Plus Real-Time PCR system (Applied Biosystems) to quantify the relative DNA copy number of *Mettl14*. *Actb* was used as internal control and relative copy number was normalized to *Actb*. To quantify mRNA level of *Ebi3*, total RNAs of $CX3CR1^+MHCII^+$ macrophages sorted from tumor-bearing WT and *Mettl14* cKO mice were extracted with miRNeasy Mini Kit (QIAGEN) according to the guidelines followed by reverse transcription using the PrimeScript RT reagent Kit (Takara) for cDNA synthesis. cDNA was used to perform qPCR with PowerUp SYBR Green Master Mix (Thermo Fisher) in a Q1 Real-Time PCR system (Applied Biosystems).

Human biopsies were collected in and stored at transport media, which consisted of Mg^{2+} and Ca^{2+} free PBS containing 50 IU/ml penicillin, 50 ug/ml streptomycin, and 0.5 mg/ml gentamycin. The biopsies were then washed three times with transport media without spinning the samples. After that 10 ml of chelating buffer, which consisted of transport media containing 1 mM EDTA and 1 mM EGTA, was added to the samples. Colonocytes from the biopsies were liberated by incubating the samples on a shaker at 4°C overnight. Next day the chelating buffer was collected in a new 15 ml tube and centrifuged at 200 g for 5 min at 4°C. The supernatant was discarded, and pellet was transferred to a microcentrifuge tube and resuspended in 0.5 ml PBS and was left on ice until combined with the colonocytes isolate from the next step. 10 ml PBS was added to the biopsies. The tube containing biopsies and PBS was shaken vigorously to allow the colonocytes to fall into suspension. The suspension was collected into a new 15 ml tube and centrifuged at 200 g for 5 min at 4°C. The supernatant was discarded and the pellet was resuspended in 0.5 ml PBS and combined with the colonocytes isolate from the previous step. To remove PBS from the colonocytes pellet, centrifugation steps were carried out for 5 min at 4°C at gradually increasing speeds for up to 7,000 rcf. The remaining biopsies lacking the colonocytes comprised the stroma part of the isolate. And then, RNA extraction was performed using TRIzol and cDNA was synthesized with PrimeScript RT reagent Kit (Perfect Real Time) (Takara) according to the manufacturer's protocol. cDNAs from human samples were then used to perform qPCR with FastStart Essential DNA Green Master (Roche).

UHPLC-MRM-MS/MS analysis of mononucleotides for m^6A level quantification

Total RNA was isolated using TRIzol and mRNA was purified using the Dynabeads mRNA Purification Kit (Invitrogen). As previously described (Yang et al., 2017), RNAs were digested in a 50 μl reaction volume containing 0.1 U Nuclease P1 (Sigma) and 1.0 U calf intestinal phosphatase (NEB) at 37°C overnight. The mixture was filtered by ultra-filtration tubes (MW cutoff: 3 kDa, Pall, Port Washington, NewYork), then analyzed to detect m^6A and rA. An Agilent 1290 UHPLC system coupled with a 6410 triple quadrupole mass spectrometer (Agilent Technologies) was used to perform the UHPLC-MRM-MS/MS analysis. UHPLC separation of mononucleotides was conducted using a Zorbax Eclipse Plus C18 column (100 mm × 2.1 mm I.D., 1.8 μm particle size, Agilent Technologies). The mass spectrometer was operated in the positive ion mode. A multiple reaction monitoring (MRM) mode was adopted: m/z 282 → 150 for m^6A and m/z 268 → 136 for rA. The injection volume for each sample was 5 μl, and the amounts of m^6A and rA were calibrated based on standard curves. Nitrogen was used as a nebulizing and desolvation gas of MS detection. The nebulization gas was set at 40 psi, the flow-rate of desolvation gas was 9 L/min, and the source temperature was set at 300°C. Capillary voltage was set at 3,500 V. High purity nitrogen (99.999%) was used as collision gas. Each sample was analyzed for at least three times.

Immunohistochemistry of human biopsies

The immunohistochemistry of human biopsies followed the protocol provided previously (Han et al., 2019) with some modifications. Briefly, to stain for macrophages (CD68, Abcam, clone: KP1) and METTL14 (Sigma-Aldrich, HPA038002), antigen retrieval was performed with 10 mM Tris base, 1 mM EDTA, 0.05% Tween 20, Ph 9. Slides were processed with the VECTASTAIN Elite ABC HRP Kit and DAB Substrate Kit (Vector Laboratories). Slides were counterstained with hematoxylin and dehydrated through graded alcohols and xylene. A total of 20 tumor samples had sufficient tissues for unambiguous analyses.

Multi-color IHC

Paraffin sections of colon cancer surgery samples were provided by Peking University Cancer Hospital & Institute followed the standardized application process. Paraffin blocks were cut into 5μm sections and adhered to glass slides. Slides were baked in the oven at 65°C for 1 hr, dewaxed with xylene, and then rehydrated through 100%, 95%, 70% alcohol successively. Multiplexed IHC was performed manually by using the Opal 7-Color Manual IHC kit (AKOYA BIOSCIENCES, NEL811001KT) according to the manufacturer' s protocol. In brief, the slide was incubated in four rounds of staining with rabbit anti-human EBI3 antibody (Abcam, clone EPR23372-282, 1:100), rabbit anti-human CD68 antibody (Abcam, clone EPR20545, 1:200), mouse anti-human CD8 antibody (Abcam, clone C8/144B, 1:100) and mouse anti-human METTL14 (Abcam, clone CL4252, 1:1000) antibody. Antigen

Please cite this article in press as: Dong et al., The loss of RNA N^6-adenosine methyltransferase *Mettl14* in tumor-associated macrophages promotes $CD8^+$ T cell dysfunction and tumor growth, Cancer Cell (2021), https://doi.org/10.1016/j.ccell.2021.04.016

EBI3, CD8, and METTL14 were retrieved by IHC Antigen Retrieval Solution 10× High pH (Invitrogen, 00-4956-58) and CD68 was retrieved by IHC Antigen Retrieval Solution 10 Low pH (Invitrogen, 00-4956-58). The slide was boiled in the microwave oven for 45 seconds at 100% power and then 15 min at 20% power, followed by blocking for 10 min at room temperature and then incubated with anti-human EBI3 antibody at room temperature for 1 hr. And then, the slides were incubated with anti-human CD68 antibody at 4°C overnight and anti-human CD8 antibody at room temperature for 3 hr, followed by incubating with anti-human METTL14 antibody at room temperature for 1 hr. The secondary antibody Polymer HRP Ms + Rb (Cat: ARH1001EA) was added and incubated at room temperature for 10 min. Signal amplification was performed using Opal Fluorophore Working Solution onto slides at room temperature for 10min. The multi-color immunohistochemistry imaging was collected by Vectra Polaris Imaging System (PerkinElmer) (Lee et al., 2020) at 20× magnification and analyzed by InForm Advanced Image Analysis Software (PerkinElmer) version 2.4.1.

RNA-seq and m^{6}A-seq

For RNA-seq of macrophage subsets, tumor-associated $CD45^+Ly6C^-CD11b^+CX3CR1^+MHCII^+$ and $CD45^+Ly6C^-CD11b^{+-}CX3CR1^-MHCII^-$ macrophages were sorted from LLC-bearing mice on day 16 by flow cytometry. For RNA-seq of total tumor-associated macrophages from LLC and B16-OVA models on day 9, $CD45^+Ly6C^-CD11b^+CD24^-MHCII^+$ macrophages were sorted. All sorted cells were conducted RNA extraction using miRNeasy Mini Kit (QIAGEN) for subsequent RNA library construction.

For m^{6}A-seq, $CD45^+CD11b^+Ly6C^-F4/80^+$ macrophages were sorted, and total RNA in macrophages was extracted. Polyadenylated RNA was purified using the Dynabeads mRNA Purification Kit (Invitrogen). Then, mRNA was fragmented into ~100-nucleotide-long fragments by 10 × Fragmentation Reagent (Invitrogen) at 94 °C for 45 s and stopped using the 10 × Stop Solution (Invitrogen). EpiMark N^6-methyladenosine enrichment kit (E1610S, NEB) was used for m^{6}A immunoprecipitation (m^{6}A-IP) to enrich the m^{6}A-marked mRNA followed by RNA extraction by TRIzol. The libraries were prepared using SMARTer Stranded Total RNA-Seq Kit (Takara) according to the manufacturer's protocol, and then we sequenced the libraries on an Illumina HiSeq X Ten platform.

Single-cell RNA-seq

Single-cell suspensions were obtained from LLC and B16-OVA-bearing WT and *Mettl14* cKO mice on day 16 and day 9, respectively. Samples were stained for 30 min using an antibody against CD45. 7-AAD was freshly added before cell sorting. $CD45^+7\text{-}AAD^-$ single cells were sorted for library construction of scRNA-seq. The libraries were performed using Chromium Next GEM Single Cell 3' GEM, Library & Gel Bead Kit v3.1 (Cat: 1000128) purchased from 10X Genomics according to the protocols provided by manufactures. The aimed target cell recovery for each library was 8,000 and the libraries were sequenced on an Illumina HiSeq X Ten platform.

Single-cell RNA-seq analysis

10X Genomics scRNA-seq data were aligned and quantified using the Cell Ranger Single-Cell Software Suit (version 3.0.2) against the mm10 reference genome. Genes with less detected cell numbers (less than 3) and cells with less detected genes (less than 200) were removed.

For single-cell data in LLC model, low-quality cells were discarded if the number of expressed genes was smaller than 500 or larger than 7,000. Cells were also removed if their proportions of mitochondrial gene expression were larger than 20%. To cluster single cells by their expression, the unsupervised graph-based clustering algorithm implemented in *Seurat* R package (version 3.1.4) was used for each data set (Butler et al., 2018). Top 2,000 variable genes identified by vst method were used to perform principal component analysis. 1-20 PCs were used in *FindNeighbors* function. The *FindClusters* function was used to determine the clusters. To identify subsets within myeloid cells, we further performed clustering for those cells.

For single-cell data in B16-OVA model, low-quality cells were discarded if the number of expressed genes was smaller than 200 or larger than 6,500. Cells were also removed if their proportions of mitochondrial gene expression were larger than 40%. To identify the cell types in WT and *Mettl14* cKO conditions, we used the integration procedure in *Seurat* R package (version 3.1.4). Briefly, top 2,000 variable genes were used to identify the anchors using *FindIntegrationAnchors* function with parameter dims = 1:20. We next integrated WT and *Mettl14* cKO datasets together with *IntegrateData* function. 1-20 PCs were used to determine the clusters. $CD8^+$ subpopulations were identified via clustering method with removing the interference of the cell cycle. To remove the interference of the cell cycle in $CD8^+$ cells, we used the cell cycle scores to regress out when scaling the single-cell data. The cell cycle genes were downloaded from the previous study (Kowalczyk et al., 2015). The cell cycle score was calculated by *CellCycleScoring* function implemented in *Seurat* package.

The markers in each subtype were calculated based on the *FindAllMarkers* function in *Seurat* package with min.pct = 0.25 and other default parameters. The information on cell types was provided in Table S1.

Ligand and receptor interaction analysis

To identify the significant and specific ligand-receptor pairs between macrophage and $CD8^+$ T cell subtypes, the CellPhoneDB tool was used in our scRNA-seq data from LLC model (Efremova et al., 2020; Vento-Tormo et al., 2018). Cell expression was normalized by dividing the total counts. The statistical method was used to analyze the normalized data. The interaction pairs were removed if the P-value = 1 or the mean attraction strength = 0. The mean attraction strength meant the average expression level of interacting molecule 1 and molecule 2. To extend the ligand-receptor pairs, we added more pairs from previous studies and implemented them in CellPhoneDB (Cohen et al., 2018; Zhang et al., 2019).

Please cite this article in press as: Dong et al., The loss of RNA N^6-adenosine methyltransferase *Mettl14* in tumor-associated macrophages promotes $CD8^+$ T cell dysfunction and tumor growth, Cancer Cell (2021), https://doi.org/10.1016/j.ccell.2021.04.016

Trajectory interference

Two different algorithms, URD and diffusion map, were used to infer the developmental trajectory of monocyte and macrophage in scRNA-seq data from LLC model.

The *URD* R package (version 1.1.1) was used to construct the trajectory into a tree structure (Farrell et al., 2018). 10% of cells randomly selected from monocytes were set as root. The trajectory analysis was applied based on the parameters with divergence.method = "preference", cells.per.pseudotime.bin = 25, bins.per.pseudotime.window = 8, and p.thresh = 0.001.

The diffusion map analysis was performed with scanpy toolkit by setting the nneighbors = 30 to compute the neighborhood graph and other default parameters (Wolf et al., 2018). When focusing on the trajectory within specific cell types, the diffusion map analysis was performed in $CD8^+$ T cells and myeloid cells. To infer the expression trends along the diffusion components, each component (1 and 2) were classified to 100 bins. Cells belonged to the monocytes to $C1q^+$ Mac or monocytes to $PTGS2^+$ Mac were placed to component 1 bins or component 2 bins, respectively. Gene expression level of each bin was calculated by averaging the normalized expression level of cells in bin. The expression trends of each gene were inferred by the loess regression model to predict the expression pattern along with the components.

Gene co-expression module analysis

To analyze the complex gene expression pattern in $CD8^+$ T cells, the correlations of top variance genes obtained from single-cell clustering step by *Seurat* R package were calculated with Spearman method. To identify the gene co-expression module, a hierarchical clustering method with complete distance was used for the correlation matrix of top variance genes. Six co-expression modules were obtained. Gene expression data were normalized by "LogNormalize" method in *Seurat* R package. The z-score transformed normalization data were then used to calculate the correlations of top variance genes. To define the transcriptional scores for progenitor state, exhaustion state, and proliferation state, we identified gene sets that were top 20 correlated with anchor genes (*Tcf7*, *Nr4a3*, and *Tox*) based on the Spearman correlation in each module. The score was calculated by averaging the normalized expression of genes in each set.

Bulk RNA-seq analysis

The adaptor sequences were first trimmed from sequencing reads by Trim Galore! (version 0.6.0) with "–clip_R1 3" and other default parameters (http://www.bioinformatics.babraham.ac.uk/projects/trim_galore/). Trimmed reads mapped to ribosomal RNA were removed using Bowtie2 (version 2.3.5) (Langmead and Salzberg, 2012). All remaining reads were mapped to the mouse genome mm9 using STAR (version 2.7.0f) (Dobin et al., 2013). Uniquely mapped reads were selected using SAMtools (version 1.9) with mapping quality $\geq$ 20 (Li et al., 2009). The gene expression raw counts were calculated using *featureCounts* function in Bioconductor *Rsubread* package (version 2.0.1) (Liao et al., 2019). Genes with differential expression were detected using Bioconductor *DESeq2* package (version 1.26.0) (Love et al., 2014). The differentially expressed genes were provided in Table S3.

For RNA-seq in the human tumor stroma, single-end RNA-seq data were mapped to the human genome hg19 using STAR. And the gene expression raw counts were calculated using htseq-count in Python (Anders et al., 2015). TPM (Transcripts Per Million) normalized data were used to calculate the overall expression of signatures in $CD8^+$ Teff and $CD8^+$ Tex subpopulations through the method mentioned previously (Jerby-Arnon et al., 2018). The signatures of $CD8^+$ Teff and $CD8^+$ Tex subpopulations were obtained in B16-OVA single-cell data by *FindAllMarkers* function in *Seurat* package with min.pct = 0.25 and other default parameters. Comparing the overall expression of subpopulations signatures between m^6A high and low groups (cutoff: m^6A/A (%) < 0.3), to avoid the interference of other cell types, the signature was selected when the expression was high in CD8 cells (average level of z-score expression was larger than 0) based on the B16-OVA single-cell data. Top 5 signatures in each $CD8^+$ T cell subpopulation were used to calculate the overall expression in tumor stroma RNA-seq data.

m^6A-seq analysis

Raw sequencing reads were trimmed by Trim Galore! followed by adjusting the parameter "–clip_R1 3". Remaining trimmed reads were aligned to the mouse genome mm9 by STAR (version 2.7.0f) (Dobin et al., 2013). Uniquely mapped reads were selected using SAMtools (version 1.9) with mapping quality $\geq$ 20 (Li et al., 2009). The m^6A-enriched regions (peaks) in each sample were detected by *exomePeak* R package (version 2.16.0) (Meng et al., 2013, 2014) with default parameters. Biological replicated peaks were considered as high-confidence peaks and merged by bedtools (version 2.28.0) (Quinlan and Hall, 2010). The significantly differential peaks between *Mettl14* cKO and WT data were defined by the thresholds of FRD $\leq$ 0.01 and $|\log_2(\text{fold change})| > 0.25$, through differential analysis in *exomePeak*. The peak annotation and binding motif were analyzed by HOMER (Heinz et al., 2010). Motif length was set to 5 and 6 nucleotides. Metagene plot was created by the Bioconductor *GUITAR* package (version1.14.0) using merged peaks from *Mettl14* cKO and WT data, respectively (Cui et al., 2016). The differential m^6A peaks were provided in Table S4.

TCGA expression data analysis

Gene expression and clinical data for lung adenocarcinoma (LUAD) were downloaded from The Cancer Genome Atlas (TCGA). Samples without survival information were excluded. 500 patients were used to infer myeloid cell type abundance in LUAD. Patients were stratified to high and low groups based on the expression level of $PTGS2^+$ Mac signatures (*ERO1A*, *HILPDA*, *SMOX*, *THBS1*, *IER3*, *PTGS2*, *SLPI*, *SDC1*, *IFITM1*, *IFITM2*, and *IFITM3*) or $C1q^+$ Mac signatures (*CD63*, *PLTP*, *C1QA*, *C1QB*, *C1QC*, *CD74*, *HLA-DQB1*,

and *HLA-DQB2*) via K-means clustering method (K = 3). Specifically, for $PTGS2^+$ Mac, 310 of the 500 patients were grouped into high or low effector $CD8^+$ T cell infiltration groups, including 225 high infiltration and 104 low infiltration patients; for $C1q^+$ Mac, 305 of the 500 patients were identified as high or low effector $CD8^+$ T cell infiltration group, including 214 high and 91 low effector $CD8^+$ T cell infiltrating patients. The effector $CD8^+$ T cell infiltration scores for patients in two groups were calculated as the overall expression (as described in **Bulk RNA-seq analysis**) of *GZMA*, *GZMB*, *CD8A*, *CD8B*, and *PRF1* (Jiang et al., 2018). The P value was calculated by Wilcoxon rank-sum test.

Public single cell data analysis

Processed scRNA-seq datasets and cell annotation from melanoma and non-small cell lung cancer (NSCLC) were downloaded from Gene Expression Omnibus (GEO: GSE120575 and GSE131907). The myeloid cells (monocyte and macrophage) and CD8 T cells were processed for dimension reduction and unsupervised clustering using *Seurat* R package (version 3.1.4) in melanoma and NSCLS, respectively. Samples with low myeloid cells (< 10) were removed. The markers in each subset were calculated based on the *FindAllMarkers* function in *Seurat* package with min.pct = 0.25 and other default parameters. The gene expression pattern from monocyte to $C1q^+$ Mac was analyzed using *monocle* R package (Trapnell et al., 2014).

QUANTIFICATION AND STATISTICAL ANALYSIS

Statistical analysis was done using GraphPad Prism 7.0 and presented as mean values ± SEM. For comparison of two groups, one-tailed or two-tailed, unpaired, *t*-test was performed to calculate p values. For cumulative distribution, the two-tailed Kolmogorov-Smirnov test was used to calculate p values. The specific test for each dataset was indicated in the figure legends. Statistical significance was denoted with (non-significant (ns), $P \geq 0.05$; *$P < 0.05$; **$P < 0.01$; ***$P < 0.001$) in the figures and figures legends.